SPECTROSCOPIC ANALYSIS OF CA-CARBONATES FROM UTAH CRYSTAL GEYSER TO SUPPORT CARBONATE DETECTION WITHIN OUR SOLAR SYSTEM

By

Z. Uriah Wolf

A thesis submitted to the Faculty of Graduate Studies in partial fulfillment of the requirements for the Master of Science degree.

Department of Environmental Studies and Sciences and Department of Geography
Master of Science in Environmental Science and Social Change
The University of Winnipeg
Winnipeg, Manitoba, Canada
May 2023

Abstract

This study investigated the Utah Crystal Geyser, a unique low-temperature, CO_2-rich geyser relevant to Mars, icy moons, and asteroids. Samples from the site had a range of textural and color differences; however, they contained similar mineral assemblages dominated by carbonates (calcite and aragonite). The identification of calcite and aragonite is important as they can be biogenically produced and possess the ability to preserve biogenic fingerprints and entomb microbial fossils.

This analysis confirmed that the most effective method for identifying and distinguishing calcite and aragonite is through a combination of several techniques. Specifically, reflectance spectroscopy was able to determine the presence of calcite-aragonite mixtures. However, it could not effectively differentiate between the two since the band positions and shapes change subtly with varying abundances of the two carbonates. Thus, it can only be stated that a mixture is present, and the degree to which transformation from aragonite to calcite has proceeded is poorly constrained. Raman spectroscopy was able to identify both calcite and aragonite and could differentiate between the two through diagnostic peaks in the low Raman-shift region of the spectrum. Scanning electron microscopy imaging provided sub-micrometer images of textures and sedimentary fabric, such as laminations, crystal structures, and entombed microbial fossils. X-ray diffractometry and X-ray fluorescence were used to determine and verify the mineralogy of the samples.

The low-temperature origin of these carbonates is likely the factor responsible for the lack of homogeneity within the samples. Carbon dioxide degassing is likely the primary factor supporting the precipitation of aragonite at the geyser, despite the low temperature. The results have implications for carbonate detection and characterization on Mars and the recognition of low-temperature carbonate precipitates on a number of planetary bodies.

Keywords: Calcite, Aragonite, Astrobiology, Biosignatures, Perseverance rover, Mars spectroscopy.

Co-Authorship Statement

This thesis is based on a manuscript that will be submitted for publication in the Planetary and Space Science Journal. I, Uriah Wolf, led the definition of the research problem, sample analysis, data analysis, interpretation of results, and writing of the manuscript and will be the lead author. Ed Cloutis, Sally Potter-McIntyre, Dan Applin, Nathalie Turenne, and Stanley Mertzman contributed to the sample collection (Ed Cloutis), data analysis, and interpretation of results and provided editorial guidance on the writing of this thesis and will be co-authors on the manuscript.

Table of Contents

List of Tables

List of Figures:

1.0 Introduction

One of the primary goals of exploring Mars is to find evidence of extinct or extant life (Hoehler & Westall, 2010; McLennan et al., 2012; Farley et al., 2020). Current exploration of Mars involves orbiters, landers, and rovers, with a recent addition, the Perseverance rover, providing unique spectrophotometric and other analytical capabilities (Ehlmann et al., 2008; Farley et al., 2020). Previous research has demonstrated the need for integrated observations across a range of scales (macroscopic to microscopic) along with spectroscopic investigations of targets that may be encountered on Mars, as Mars has a geologically diverse terrain (McLennan et al., 2012).

Landed Mars missions have transformed our understanding of Mars and have shown that it was once much more habitable (e.g., Grotzinger et al., 2012). Exploration and the derived knowledge of Mars can be informed by research conducted at terrestrial Mars analogue sites; such sites are locations on Earth that are relevant to Mars in one or more aspects, such as geology, or provide information regarding mechanisms that may have assisted in the preservation of possible microbial fossils on Mars.

In the latter application, fossil biosignatures preserve evidence of ancient life, and substantial information can be obtained from them. Their formation within the biosphere involves interactions between the atmosphere, lithosphere, and hydrosphere and the resulting processes, such as degradation, preservation, transformation, and mineralization, that affect physiochemical properties (e.g., Hays et al., 2017 and references therein). Mars analogue sites, such as the Utah (USA) Crystal Geyser deposit described below, are appropriate locations to better understand microbial ecosystems and preservation, as well as their role in the mineralization process. As carbonates are widely present across Mars (e.g., Morris et al., 2010; Goudge et al., 2015, 2017; Horgan et al., 2020; Boynton et al., 2021; Tarnas et al., 2021), exploring terrestrial carbonate analogues can inform the search for, and characterization of, similar environments on Mars.

1.1 Carbonates: Formation conditions

Carbonates are a class of minerals that can be used to record past environmental conditions, as their formation is dependent on prevailing physicochemical conditions, and their ongoing preservation can depend on subsequent environmental conditions (Tarnas et al., 2021). This makes carbonates of particular interest in understanding Mars's potential habitability and astrobiological potential. Carbonates can form under a wide range of environmental conditions and are sensitive to factors such as temperature, varying ion activity in solution, or carbon dioxide (CO_2) levels (Hays et al., 2017). An increasing amount of evidence suggests that amorphous calcium carbonate can be a precursor in the biomineralization process (Faatz et al., 2004). Faatz et al. (2004) suggests that precipitation of amorphous calcium carbonate as a transient species can support the formation of complex living systems despite being a physically unstable intermediate.

In the case of calcium carbonate ($CaCO_3$), there are three anhydrous crystalline polymorphs: vaterite, aragonite, and calcite (Rao, 1973; Ogino et al., 1987; Parker et al., 2010; Xu & Sommerdijk, 2018). Vaterite is not thermodynamically stable and is, therefore, very rare in nature, while calcite is the most stable and is widely present in rocks or as biominerals (Xu & Sommerdijk, 2018). Vaterite precipitates at a temperature of approximately 25°C, much lower than aragonite and calcite, which precipitate at approximately 70°C and 80°C, respectively (Ogino, 1987; Beruto & Giordani, 1993; Vecht & Ireland, 2000). The rate of transformation is dependent on temperature and time, taking about 60 minutes for vaterite to transform into aragonite at 50°C (Ogino et al., 1987); however, vaterite can also transform directly into calcite at higher temperatures (Rao, 1973). Vaterite seems to be more stable in some biological systems (e.g., Meenakshi et al., 1974; Oliveira et al., 1995; Giralt et al., 2001; Palchik & Moroz, 2005). At standard temperature and pressure and with a highly supersaturated solution of Ca^{2+} and CO_3^{-2} ions, amorphous calcium carbonate (vaterite, aragonite, and calcite) will rapidly precipitate (Ogino et al., 1987).

Aragonite crystallization often occurs in environments such as limestone caves or biogenically in marine environments (Ford, 2006; Parker et al., 2010; Zhang et al., 2020). Invertebrates such as

corals, gastropods, and mollusks precipitate aragonite to form their shells or skeletons. Aragonite's micro-architecture allows it to withstand changes in environmental conditions (Ren et al., 2009; Parker et al., 2010; Casella et al., 2017; Xu & Sommerdijk, 2018). On a smaller scale, several species of bacteria can precipitate aragonite due to their cell surface structures and metabolic activity (Zhang et al., 2019; Khan et al., 2021). Cyanobacteria can enable the formation of aragonite laminations via metabolic processes and can form macroscopic structures when present as microbial mats (Okumura et al., 2012). Laminated travertine can occur from glutinous extracellular polymeric substances (EPS) trapping detritus and which also provide a substrate on which $CaCO_3$ can nucleate (Takashima et al., 2011). They can also inhibit crystal growth by binding cations (Takashima et al., 2011). Records of past environmental conditions can be identified from structural features formed in aragonite that is left behind by living organisms (Beruto & Giordani, 1993; Casella et al., 2017).

Aragonite, normally a high-pressure polymorph or bioprecipitate, is metastable at low temperatures and ambient pressure (McTigue & Wenk, 1985; Parker et al., 2010). Aragonite commonly transforms into calcite, the most stable form of calcium carbonate, via an endothermic and irreversible reaction (Ogino et al., 1987; Parker et al., 2010). The transformation occurs through nucleation and growth mechanisms that arise from atomic displacements (Parker et al., 2010), and can allow for sub-micrometer scale preservation of morphologies (Beruto & Giodani, 1993). Many studies have been done to understand the transformation process from aragonite to calcite (e.g., Fraust, 1950; Gruver, 1960; Brown et al., 1962, and many more). The rate of aragonite transformation to calcite depends on temperature, taking only a few minutes at temperatures over 400°C or a few days at temperatures between 50 to 100°C (McTigue & Wenk, 1985; Ogino et al., 1987; Parker et al., 2010). Biogenic aragonite transforms into calcite at lower temperatures than abiogenic aragonite due to structural differences in the crystallographic orientation, affecting its ability to alter physically (Ren et al., 2009; Parker et al., 2010). In addition, higher magnesium content slows the rate of transformation, as it inhibits calcite nucleation and also results in larger calcite crystals (Beruto & Giordani, 1993).

By examining carbonates at terrestrial analogue sites we can gain insights into the conditions that allow for the formation, transformation, and preservation of specific carbonates. This is key to evaluating past habitability and potential for biosignature preservation on Mars.

1.2 Carbonates on Mars

Carbonates have been detected orbitally in several different Mars localities by the Compact Reconnaissance Imaging Spectrometer for Mars (CRISM) instrument on the Mars Reconnaissance Orbiter (MRO) (Ehlmann et al., 2008; Ehlmann et al., 2009; Ehlmann et al., 2010; Morris et al., 2010; Cater & Poulet, 2012; Goudge et al., 2015, 2017; Bramble et al., 2017; Horgan et al., 2020; Boynton et al., 2021; Tarnas et al., 2021), including Jezero Crater, the current location of the Perseverance rover (Goudge et al., 2015, 2017; Horgan et al., 2020; Tarnas et al., 2021). Recent geologic mapping has identified carbonate-bearing units in the northern regions of Jezero crater (Stack et al., 2020), and Mg-rich carbonates such as magnesite have been detected within the Jezero crater paleolake basin by CRISM (Goudge et al., 2015). The Planetary Fourier Spectrometer onboard the Mars Express Orbiter identified carbonates in both bright and dark regions of the Mars surface, with an abundance reaching ~10 wt. % (Palomba et al., 2009). Mg-carbonate was detected in the Nili Fossae region on Mars by CRISM (Ehlmann et al., 2008).

Calcite has been identified by the Thermal and Evolved-Gas Analyzer (TEGA) and the Microscopy, Electrochemical, and Conductivity Analyzer (MECA) instruments on the Phoenix Lander at concentrations of approximately 3 to 5 weight percent (Boynton et al., 2009). The Curiosity rover has detected trace amounts of carbonates in eolian material (Bridges et al., 2018). Fe-carbonate was identified by the CheMin X-ray diffraction instrument on board the Curiosity rover in the Glen Torridon region of Gale crater (Bennett et al., 2022). A study by Zastrow and Glotch (2021) shows modeling that supports the presence of calcite associated with the sandy regions within the Marginal Carbonate unit in Jezero crater.

Iron- and magnesium-rich carbonates have also been identified in Martian meteorite Allan Hills 84001 found in Antarctica (Borg et al., 1999; Golden et al., 2001; Steele et al., 2007) and appear

similar to the carbonates in Comanche outcrop in the Gusev crater on Mars (Niles et al., 2013). Calcite has also been detected in four of the six known nakhlite Martian meteorites (Hicks et al., 2014) and Shergotty (Gibson et al., 2001).

There have been many hypotheses about how carbonates have formed on Mars, and multiple processes may likely have occurred. Carbonate can form from water and basalt in a CO_2-rich atmosphere (Ehlmann et al., 2008) with research suggesting that due to the widespread distribution of carbonates on the surface of Mars, atmospheric water 3.7 billion years ago could have interacted with carbonate/bicarbonate ions to form carbonates (Bultel et al., 2019). In this process, carbon dioxide (CO_2) and water (H_2O) interact to form carbonic acid (H_2CO_3) which can then be deprotonated to form bicarbonate (HCO_3^-) and then carbonate (CO_3^{2-}) through acidification. The carbonate (CO_3^{2-}) ions can interact with calcium (Ca^{2+}) ions to form calcium carbonate ($CaCO_3$). It is suggested that the carbonates may have precipitated rapidly under low-temperature conditions through inorganic processes in non-equilibrium solutions (Golden et al., 2001). Precipitation of carbonates likely occurred from CO_2-rich flowing water, which was present on ancient Mars, followed by a transient thermal event such as meteorite bombardment (Borg et al., 1999; Golden et al., 2001; Steele et al., 2007). Palomba et al. (2009) also suggest that carbonates may have precipitated directly from the atmosphere. Morris et al. (2010) suggest it is likely that extensive aqueous activity under neutral pH once occurred on Mars.

1.3 Carbonates on icy moons and asteroids

Both Enceladus and Europa likely have subsurface oceans (Carr et al., 1998; Kivelson et al., 2000; Orlando et al., 2005), making them potentially habitable environments (Hendrix et al., 2019). Subsurface water erupts onto the surface of these moons, which appear as plumes (geysers) in the case of Enceladus (Waite et al., 2006; Hansen et al., 2011) or diffuse concentrations or in possible plumes around Europa (Lorenz, 2016; Teolis et al., 2017; Vorburger & Wurz, 2021). The plumes are favorable targets for understanding the habitability of these moons because they provide access to subsurface materials formed in presumably more habitable environments (Lorenz, 2016; Hendrix et al., 2019). While most information available on these moons comes from modeling and limited observational data, the Cassini and Galileo

spacecraft provided extensive data concerning plume composition that improved the models (Zolotov, 2007; Glein & Waite, 2020; Vorburger & Wurz, 2021).

Plumes on both Enceladus and Europa are of interest as their composition provides insights into interior processes and composition (Glein & Waite, 2020). Cassini mass spectrometry data from the Enceladus plumes indicates that the levels of CO_2 present are compatible with long-term buffering by seafloor rocks containing quartz, talc, and carbonate minerals (Glein & Waite, 2020). Cassini data showed that the pH of Enceladus' ocean is high, around 11-12, which is compatible with life and may resemble conditions that allowed for life to evolve on Earth (Glein et al., 2015; Neveu et al., 2020). Recent findings of silica and H_2 in the plumes of Enceladus, along with reaction modeling, support the hypothesis proposed by Glein and Waite (2020) that Enceladus may have a carbonated upper mantle. A study by Cardoso et al. (2018) aimed to simulate Enceladus conditions through the use of chemical gardens and found that calcite and vaterite may form under Enceladus conditions. As it is hypothesized that life may have begun in lower-temperature alkaline hydrothermal vents, they modeled their experiments according to this geochemistry. While less is known about Jupiter's icy moon, Europa, the Galileo spacecraft provided data that suggest the existence of a subsurface ocean similar to that of Enceladus (Zolotov & Shock, 2004). The formation of Europa is also suggested to be similar to Enceladus and likely has a sulfate-carbonate-rich ocean (Zolotov & Shock, 2004).

In addition to icy moons, asteroids can also host carbonates. Ceres is the largest asteroid and has been analyzed in detail using Visible and Infrared (VISIR) spectroscopy by the Dawn orbiter. Several different carbonate minerals were identified through visible and infrared mapping (Carrozzo et al., 2018). Hydrated carbonates on the surface of Ceres indicate that their formation is recent and may be ongoing. Calcium-, magnesium-, and sodium-rich rich carbonates have been detected and are suspected of having formed from a subsurface brine solution (Carrozzo et al., 2018; Palomba et al., 2019; Raponi et al., 2019).

The Hyabusa2 spacecraft collected rock samples from the surface of 162173 Ryugu, a near-Earth C-type asteroid (Nakamura et al., 2022; Yokoyama et al., 2022; Loizeau et al., 2023; Nakato et al., 2023). Loizeau et al. (2023) found a large presence of carbonate populations such as

dolomite and breunnerite. Nakato et al. (2023) identified four regions in the Ryugu sample: dark, glossy, bright, and white, and all regions were found to contain carbonates. The dark group contains a composition similar to Mg-Ca carbonate somewhere in the dolomite compositional range, the glossy group has a dolomite composition, the bright group contains larger dolomite grains, and the white group contained large Mg-Fe carbonate grains. Nakamura et al. (2022) found Ca carbonate in the least altered fragments that they studied. Yokoyama et al. (2022) identified three types of carbonates in the fragment they analyzed, calcite, dolomite, and breunnerite. Another sample return mission, OSIRIS-REx collected rock fragments of near-Earth asteroid 101955 Bennu. While OSIRIS-REx is still on its journey back to Earth, much research has already been conducted to study this asteroid (DellaGiustina et al., 2020; Kaplan et al., 2020; Simon et al., 2020; Ferrone et al., 2020). Kaplan et al. (2020) analyzed data collected by the OSIRIS-Rex Visible and InfraRed Spectrometer (OVIRS), which detected a 3.4 μm feature associated with carbon-baring species, and they were able to determine that the band is likely associated with calcite, siderite, magnesite, dolomite, and breuunerite.

The study of the composition of asteroids and meteorites can inform the geological processes at play during the formation of the early Solar System (DellaGiustina et al., 2020; Kaplan et al., 2020; Simon et al., 2020; Ferrone et al., 2021; Nakamura et al., 2022; Yokoyama et al., 2022; Loizeau et al., 2023; Nakato et al., 2023). Carbonates such as calcite, aragonite, dolomite, siderite, and breunnerite have also been identified in carbonaceous chondrite meteorites, most commonly in the CI and CM classes (De Leuw et al., 2010; Lee et al., 2014). Meteoritic carbonates can provide a record of information about parent body processes, particularly aqueous and hydrothermal alterations (Lee et al., 2014; Kaplan et al., 2020). Carbonates were likely formed on the parent body in an aqueous environment, allowing metastable carbonates such as aragonite to form before altering into more stable polymorphs (De Leuw et al., 2010).

In this study, we have explored a unique terrestrial non-hydrothermal, CO_2-driven, and carbonate-rich analogue site to provide insights into the kinds of deposits associated with such terrains. We also used this site to search for novel mineralogical or petrological signatures and briefly explore how such terrains may entomb and preserve microbial fossils.

2.0 The Crystal Geyser, Utah, USA carbonate springs analogue site

2.1 Site Description

Crystal Geyser (38.94° N, 110.14° W) is located 14.5 kilometers south-east of Green River, Utah, USA, and is part of a natural spring system along the Little Grand Wash fault in the northern section of the Paradox Basin of the Colorado Plateau (**Figure 1**) (Barth & Chafetz, 2015; Potter-McIntyre, 2019). This system is a rare example of a man-made low-temperature geyser (Potter-McIntyre et al., 2017) created in 1935 during exploration for oil and gas in the area (Barth & Chafetz, 2015; Waltham, 2001). Unlike a typical geothermally-activated geyser, this spring system erupts due to large amounts of carbon dioxide dissolved in the groundwater and underlying gas pressure. The eruptions are bimodal and occur approximately 8 or 22 hours apart, with eruptions lasting about 100 minutes per day (Gouveia & Friedmann, 2006). The amount of water erupted has decreased significantly over the years, from over 120 m^3 in the 1970s to less than 25 m^3 today (Shipton et al., 2005; Waltham, 2001). Records from before the 1950s show that each eruption has significantly decreased in duration and volume of water erupted, which can be explained by degassing of the system over time (Shipton et al., 2005).

Figure 1: Image of the Utah Crystal Geyser with vent shown (photo credit: Dr. Sally Potter-McIntyre).

The consistent and persistent eruption of the geyser has created a gently sloping travertine mound a few meters thick consisting of precipitated carbonates, composed predominately of calcite, with aragonite increasing in concentration approaching the spring (Barth & Chafetz, 2015). The water erupted from the geyser is rich in dissolved minerals, resulting in the precipitation of dominantly carbonate minerals. The carbonate minerals that precipitate form terraces, with each major terrace being about 5 mm thick, collectively forming a thick (many meters) travertine bank (Waltham, 2001).

Before the site was drilled in 1935, there was already a natural travertine-depositing spring system in place (Potter-McIntyre, 2019; Burnside, 2010). Radiometric dating shows that this spring system has been leaking to the surface for over 400,000 years, resulting in >20-meter-thick deposits of travertine (Burnside, 2010). The well was drilled through this existing travertine, reaching the bottom of the Triassic section at around 800 meters (Baer & Rigby, 1978). A carbon

dioxide-charged aquifer that is thought to be derived from acidic groundwater reacting with Jurassic Navajo Sandstone lies at a depth of approximately 215 meters (Baer & Rigby, 1978; Waltham, 2001; Potter-McIntyre, 2019).

Water erupting from the geyser has a temperature of roughly 18°C and originates from the shallow aquifer (Potter-McIntyre, 2019). The water has a high salt content (approximately 8000 ppm salt content) (Waltham, 2001) and contributes around 2730 metric tons of Na, Ca, K, and Mg salts to the Green River annually (Baer & Rigby, 1978). The water is slightly acidic (Shipton et al., 2005) with a pH of 6.2 – 7 (Shipton et al., 2004; Potter-McIntyre et al., 2017) and is supersaturated with calcite, aragonite, dolomite, and hematite (Heath, 2004; Potter-McIntyre, 2019).

2.2 Previous studies of Crystal Geyser

The unique characteristics of Crystal Geyser have resulted in several studies on various aspects of it, such as the water chemistry (Gouveia et al., 2005; Han et al., 2017) as well as the microbial life and adaption to a CO_2-rich environment (Santillan et al., 2015; Takashima et al., 2011; Potter-McIntyre et al., 2017).

2.3 Relevance of Crystal Geyser to solar system bodies

Since hydrothermal springs are a common occurrence on Earth, there have been several studies on their associated mineralogy (e.g., Renaut & Jones, 1997; Canet et al., 2003; Smith et al., 2011; Horton et al., 2012; Zentilli et al., 2019, and many others). Terrestrial low-temperature, CO_2-driven geysers are rare and provide novel insight into the mineralization and preservation of microbial life in such environments. Our study provides insights into such environments and the ability of such springs to preserve microbial communities. As mentioned, the results of this study may be useful in identifying the formation conditions of carbonates on Mars, icy moons, and asteroids such as Ceres, and their astrobiological potential.

For relatively cold planetary surfaces such as Mars, Enceladus, Europa, and Ceres, Crystal Geyser may be more relevant than hydrothermal geysers as it is a low-temperature and CO_2-driven spring. Crystal Geyser is an exceptional site for the entombment and preservation of microbial fossils and

other biosignatures and for evaluating diagenetic alteration of biosignatures (Potter-McIntyre et al., 2017). Rapid mineral precipitation and microbial processes interact with each other, making this a favorable environment for better understanding carbonate formation and transformation, biosignature production and preservation, and microbial fossilization (Cady & Farmer, 1996; Knuth & Potter-McIntyre, 2019).

Crystal Geyser is known to host microbial life such as *Leptothrix ochracea* or similar bacterium; however, the levels of salinity present are too high for other life forms (Baer & Rigby, 1978; Potter-McIntyre et al., 2017; Potter-McIntyre, 2019). Microbes enhance mineral precipitation and affect mineral deposits, as they can mediate chemical and mineralogical composition (Cady et al., 2003; Potter-McIntyre, 2019). Several of the unique features found at Crystal Geyser can be attributed to microbe presence, including the green and orange color of the pools and the terracettes (Emerson et al., 2016; Potter-McIntyre et al., 2017).

The investigation of terrestrial low-temperature springs is relevant to Mars because the spring system is rich in CO_2 and because of the geyser's ability to host and preserve life (e.g., Allen & Oehler, 2008). Although carbonates have been identified at several locations on Mars, their formation conditions are generally poorly constrained (e.g., (Ehlmann et al., 2008; Palomba et al., 2009; Ehlmann et al., 2009; Ehlmann et al., 2010; Morris et al., 2010; Cater & Poulet, 2012; Goudge et al., 2015, 2017; Bramble et al., 2017; Horgan et al., 2020; Boynton et al., 2021; Tarnas et al., 2021). Similar to possible habitable environments on icy moons, Crystal Geyser hosts microbial life that has adapted to life in the deep carbon dioxide- and saline-rich waters (Emerson et al., 2016; Knuth & Potter-McIntyre, 2019). Researching sites like Crystal Geyser can provide useful information for future missions to planetary bodies that may host similar subsurface environments. In addition, improving the detection, characterization, and differentiation of biologically significant minerals such as calcite and aragonite is important to guide space missions.

This study aims to 1) differentiate between calcite and aragonite in spectra obtained from instruments that are relevant to the Mars Curiosity and Perseverance rovers, and instruments onboard other spacecraft using samples collected from an analogue site, Utah Crystal Geyser, that is relevant to other planetary bodies such as Mars, icy moons, meteorites, and asteroids. 2) compare

reflectance spectra of laboratory prepared mixtures of calcite and aragonite with reflectance spectra collected on the Utah Crystal Geyser samples to understand how band depth and shape change with varying aragonite weight percentages.

3.0 Materials and Methods

3.1 Sample descriptions

Samples collected from the Crystal Geyser site were obtained at various distances from the vent pipe but are all surficial samples. The samples likely vary in age and the extent of alteration they have undergone because of the temporally changing discharge flow paths. Spectroscopic analysis of samples obtained was used to identify the mineralogy of the deposits and any characteristics unique to low-temperature, CO_2-driven carbonate deposits. Spectroscopic analysis was supplemented with data obtained for the samples using other analytical techniques.

The samples collected from the Crystal Geyser site are shown in **Figures 2 and 3**. Sample numbers with their corresponding descriptions are provided in **Table 1**. All samples were air-dried for a few weeks to minimize any easily adsorbed water.

Figure 2: Images of the samples collected from Utah Crystal Geyser. Sample numbers are noted from UTE001 to UTE011 (see **Table 1** for descriptions). Scale bar is in increments of 1 cm.

Figure 3: Sample UTE005 cut in half to show internal layering. Sample is 20 mm wide and 14 mm high.

Table 1: Crystal Geyser, Utah samples.

Sample Number	Sample Description
UTE001	Roughly laminated silica sinter (red-orange stained), with embedded clasts; ~5 meters from the borehole.
UTE002	Roughly laminated silica sinter (red-orange stained), with embedded clasts; ~5 meters from the borehole.
UTE003	Five silica nodules (spherical to oblate; red-orange); ~4 meters from the borehole.
UTE004	Light-toned terrace deposit; ~30 meters downhill from the borehole.
UTE005	Loose nodules next to borehole; <1 meter away.
UTE006	Yellow-orange loose granular materials on the surface closest to the borehole; 15 cm away.
UTE007	White surface precipitates furthest from borehole; ~40 meters from the borehole.
UTE008	Extracted surface sample of yellow terrace; ~10 meters from the borehole.
UTE009	Extracted surface sample of red terrace close to geyser; ~2 meters from the borehole.
UTE010	Extracted friable, light-toned porous surface sample close to borehole; ~3 meters away.
UTE011	Extracted surface sample from yellow terrace, midway downstream; ~20 meters from the borehole.

3.2 Analytical procedures and instrument descriptions

Each sample was analyzed as a whole rock, including weathered exterior surfaces, broken fresh surfaces, and polished interior surfaces, when available, and powders, using various techniques described below. Subsamples were also crushed to <45 μm powders for analysis by X-ray diffractometry (XRD), X-ray fluorescence (XRF), and wet chemistry (WC; for ferrous-ferric iron determination). The polished interior samples were also analyzed by scanning electron microscopy with energy dispersive spectroscopy (SEM+EDS), providing data relevant to the planetary instrument for X-ray lithochemistry (PIXL) instrument on the Perseverance rover (Wade et al., 2016; Allwood et al., 2020). The powders used for XRF and XRD were prepared by hand-crushing the samples in an alumina mortar and pestle until the entire sample was reduced to <45 μm grain size. Subsamples were also crushed to <1000 μm for analysis by reflectance and Raman spectroscopy. The analytical techniques applied to the samples, and the identified phases, are provided in **Table 2**. The XRD analyses are comparable to that provided by the CheMin instrument on the Curiosity rover (Blake et al., 2012), while the elemental analyses are comparable to data

acquired the ChemCam and APXS instruments on the Curiosity rover (Wiens et al., 2012; Campbell et al., 2019) and by the SuperCam laser-induced breakdown spectrometer (LIBS) and PIXL elemental analyzer on the Perseverance rover (Wade et al., 2016; Fouchet et al., 2021; Allwood et al., 2020). Reflectance spectra are relevant to multiple instruments on the Perseverance rover (Mastcam-Z, SuperCam – Buz et al., 2019; Bell et al., 2021; Fouchet et al., 2021; Maurice et al., 2021), the Curiosity rover (Mastcam – Bell et al., 2017), and Rosalind Franklin rover (PanCam, ISEM, Ma_MISS, MicrOmega – Josset et al., 2017; Martinez et al., 2018; Allender et al., 2021), while Raman spectroscopy is relevant to the SHERLOC and SuperCam instruments on the Perseverance rover (Beegle et al., 2015; Bhartia et al., 2021; Fouchet et al., 2021; Maurice et al., 2021) and the RLS on the Rosalind Franklin rover (Veneranda et al., 2020). Visible light images were acquired on the exterior, broken, and polished surfaces using a Canon Eos M200 camera equipped with a 6000 x 4000-pixel detector.

3.2.1 X-ray diffraction (XRD)

XRD characterization of the samples was done using <45 μm powdered subsamples. The XRD analysis acquired continuous scan data from 5 to 80° 2-theta on a Bruker D8 Advance with a DaVinci automated powder diffractometer. A Bragg-Brentano goniometer with a theta-theta setup was equipped with a 2.5° incident Soller slit, 1.0 mm divergence slit, a 2.0 mm scatter slit, a 0.2 mm receiving slit, a curved secondary graphite monochromator, and a scintillation counter collecting at an increment of 0.02° and integration time of 1 second per step. The line focus Co X-ray tube was operated at 40 kV and 40 mA, using a take-off angle of 6°. The data were analyzed using a PDF-2 database from the International Centre for Diffraction Data (IDCC) and interpreted using Bruker diffrac.eva software.

3.2.2 X-ray fluorescence (XRF) and wet chemistry and wet chemistry (WC)

Compositional analysis was carried out at Franklin and Marshall College using XRF to identify major and selected minor elements and WC to determine ferrous iron content. Details of the procedures can be found in Reichen and Fahey (1962), Govindaraju (1994), and Mertzman (2000) and online at: https://www.fandm.edu/earth-environment/laboratory-facilities/xrf-and-xrd-lab.

3.2.3 Scanning electron microscopy

A Hitachi FlexSEM 1000 II collected backscattered electron (BSE) images on uncoated samples at a working distance of ~10 mm. Variable pressure mode (30 Pa air) was used to reduce charge buildup. X-ray elemental maps were acquired using a Silicon Drift Detector (SDD) at the same working distance. Various accelerating voltages and beam currents were used, depending on the target. The BSE and X-ray maps were used to characterize variations in composition within the samples. The samples were carbon-coated for analysis, so maps of carbon content were not representative of true carbon content; however, maps of other dominant elements were produced. The BSE images were analyzed in conjunction with the elemental maps to understand the textural-compositional properties of the samples.

3.2.4 Reflectance spectroscopy

An Analytical Spectral Devices (Boulder, CO) LabSpec 4 Hi-Res® spectrophotometer collected reflectance spectra from 350 to 2500 nm at a viewing geometry of i=30° and e=0°. An in-house 150 W tungsten light source provided incident lighting with a divergence angle of <1.5°. A total of 500 spectra per sample, standard, and dark current were acquired and averaged to improve the signal-to-noise ratio (SNR). The spectrometer collects data with a spatial resolution of between 2 and 7 nm and a spectral sampling interval of 2.2 nm, which is then internally resampled by the spectrometer to output data at 1 nm intervals. The spectra were corrected for dark current and small absorption features beyond 2 μm in the absolute reflectance of Fluorilon®, as well as occasional small reflectance offsets at 1000 and 1830 nm, where detector changeovers occur. Data in the figures are reported in terms of absolute reluctance relative to Fluorilon® which wasused as the standard. Laboratory spectra were acquired, both as whole rocks on exterior surfaces, broken surfaces, and polished surfaces, after which interior subsamples were crushed to <45 an <1000 μm. Whole-rock spectra were acquired with a spot size of ~25 mm diameter on desired surfaces.

A continuum removal (modeled as a mathematical function) was calculated for several spectra on each sample to isolate a particular absorption feature, determine the band center, and better view the band shape. A continuum was removed by dividing the reflectance spectrum from the apparent absorbance using a straight-line continuum tangent to the reflectance spectrum on either side of an

absorption feature of interest and then fitting a Gaussian function to desired absorption feature using apparent absorbance versus photon energy (Clark & Roush, 1984).

3.2.5 Raman spectroscopy

A Metrohm-BWTek BWS415 iRaman spectrometer with a 532 nm laser was used to characterize the sample surfaces. The laser is coupled to a silica fiber optic bundle and passed through a quartz focusing lens, which achieves a spot diameter of ~85 μm full width half maximum (FWHM) while in focus. The Raman scattered light is collected through the quartz lens, transmitted through an OD6 notch filter to remove the Rayleigh line, then coupled to a silica fiber. The Raman scattered light is transmitted through a collection slit onto a diffraction grating, and the light is then measured with a linear array CCD thermoelectrically stabilized at 14°C. This setup achieves a sampling interval of 2.85 Δcm^{-1} at 172 Δcm^{-1}, 1.45 Δcm^{-1} at 4002 Δcm^{-1}, and a spectral resolution of roughly 4 Δcm^{-1} FWHM. The system covers the spectral range of 175 to 4000 Raman shift (Δcm^{-1}). A laser power of 50 mW was used, and various integration times were used, depending on the Raman scattering and fluorescence of the samples, to achieve optimal SNR. The Raman spectra were relative intensity corrected, per ASTM E2911 – 13. Raman spectra were collected on the same surfaces as the reflectance spectra. The data were analyzed by identifying peak positions and interpreting them using the Ruff database (https://rruff.info/).

4.0 Results

4.1 Reflectance spectroscopy

Reflectance spectra were collected on whole-rock exterior weathered surfaces and freshly broken interior surfaces, and identified phases are provided in **Table 2**. The reflectance spectra on each sample consistently exhibited absorption bands near 1400 and 1900 nm due to OH/H_2O (1400 nm) and H_2O (1900 nm). Band depths varied for each sample depending on water/hydroxyl content and varied between spectra of exterior weathered surfaces versus fresh interior surfaces. Exterior versus interior surfaces have different textures, which can affect albedo and, therefore, the depth of the absorption bands. Some of the samples had very clear visible layering (e.g., UTE008), but the spectra collected on different layers only varied in terms of color, albedo and depth of the iron

oxyhydroxide absorption band (**Figure 4d**). Every sample collected from this site exhibits a broad, variable-intensity absorption band around ~900 nm, which is characteristic of iron oxyhydroxides (Scheinost et al., 1998). The band depth varies roughly depending on the iron content of the sample. This band is very prominent for UTE009 but hardly exists for UTE007 due to the surface of this sample having a thick white, iron-free, coating (**Figure 4b**).

The reflectance spectra for samples UTE004, UTE006, UTE009, UTE010, and UTE011 exhibit a faint absorption feature near 675 nm which is characteristic of chlorophyll (**Figure 4a**) (Das et al., 2005; Wolfe et al., 2006). Samples UTE001, UTE002, UTE005, and UTE010 show a shallow absorption feature around ~2200 nm, which is indicative of the presence of silica (**Figure 4c**) (Rice et al., 2013). This aligns with the XRD data, which indicated the presence of quartz/silica in these samples.

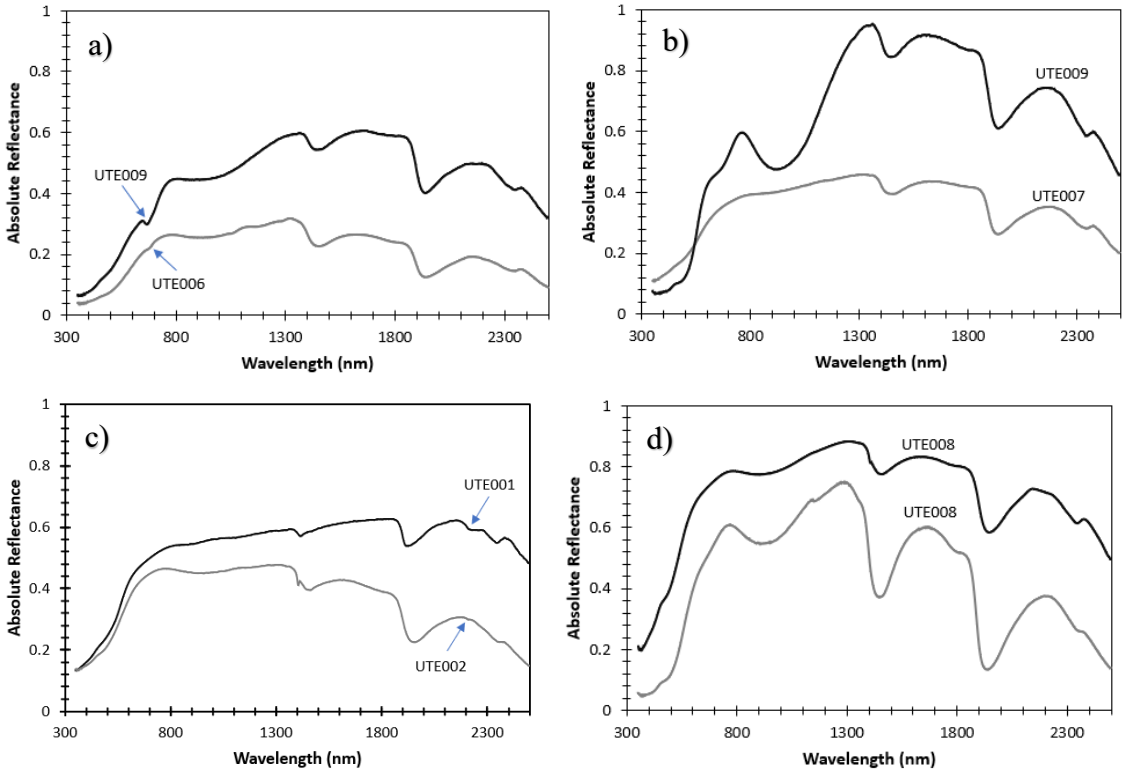

Figure 4: Reflectance spectra (350-2500 nm) for (a) UTE009 and UTE006 show a faint absorption feature near 675 nm that corresponds to chlorophyll. (b) UTE009 and UTE007 show significant variations in the iron oxyhydroxide absorption feature in the <1000 nm region, including spectral slope in the <500 nm region and absorption feature near 900 nm. (c) UTE001 has the highest concentration of silica – seen as an absorption feature in the 2200 nm region (see **Table 4**) as opposed to the UTE002 spectrum, where it is essentially absent. (d) UTE008 showed several well-defined layers; upon analysis, the color change corresponds to varying concentrations of iron oxyhydroxides; the other spectral features are largely invariant.

The reflectance spectra for each sample exhibited an absorption band around 2350 nm, which is consistent with carbonates (Gaffey, 1985, 1987). This band is associated most closely with calcite and aragonite, but they are not easily distinguishable from each other in the sample spectra due to their closely overlapping absorption bands. The spectra also lack additional lower wavelength C-O overtones and combination absorption bands that could allow for better differentiation between calcite and aragonite. A continuum was removed for all sample spectra to allow for the center of the carbonate absorption feature in the 2350 nm region to be determined for each spectrum. However, since the band positions and shapes change subtly with differing concentrations of the

two carbonates and varying grain size, as seen in **Figure 5**, it can only be stated that a mixture is present, and the degree to which transformation has proceeded is poorly constrained. From these mixtures, it appears that calcite dominates this spectral region with concentrations >~30 wt. %. **Figures 6 and 7** show the continuum removed 2350 nm region absorption feature for sample UTE001. Comparing the shape of the adsorption band in **Figure 6** to the bands shown in **Figure 5**, it is clear that this specific part of the sample is calcite-rich due to its shape. Comparing **Figure 7** to the bands in **Figure 5**, this part of the sample is more aragonite dominant. Generally, when comparing the band shape of the continuum-removed spectra, a mixture of calcite and aragonite is a consistent trend among all samples.

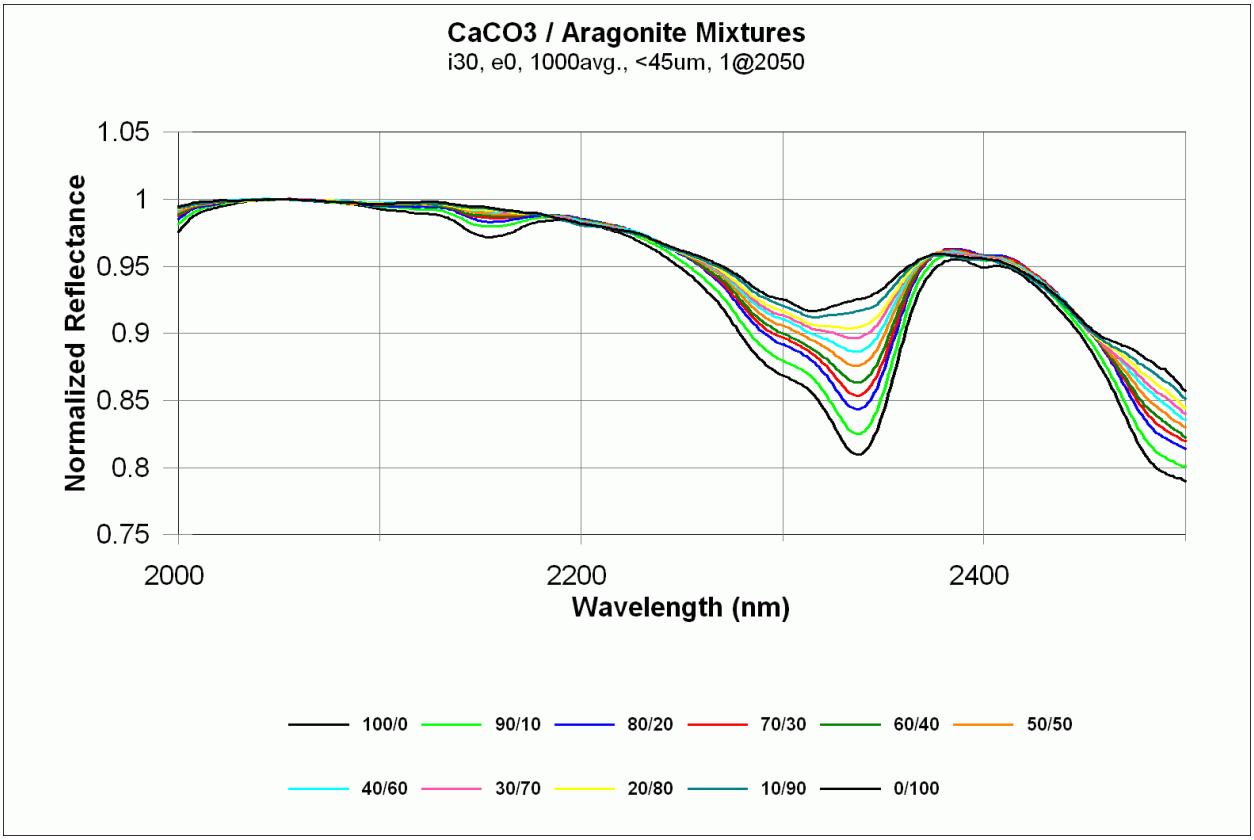

Figure 5: Reflectance spectra, normalized to 1 at 2050 nm, of 10% by-weight mixtures of calcite and aragonite. Following a line from bottom to top at ~2330 nm, the bottommost spectrum is 100% calcite, with aragonite content increasing by 10% for each spectrum as it steps up to 100% aragonite in the topmost spectrum (adapted from Craig, 2010).

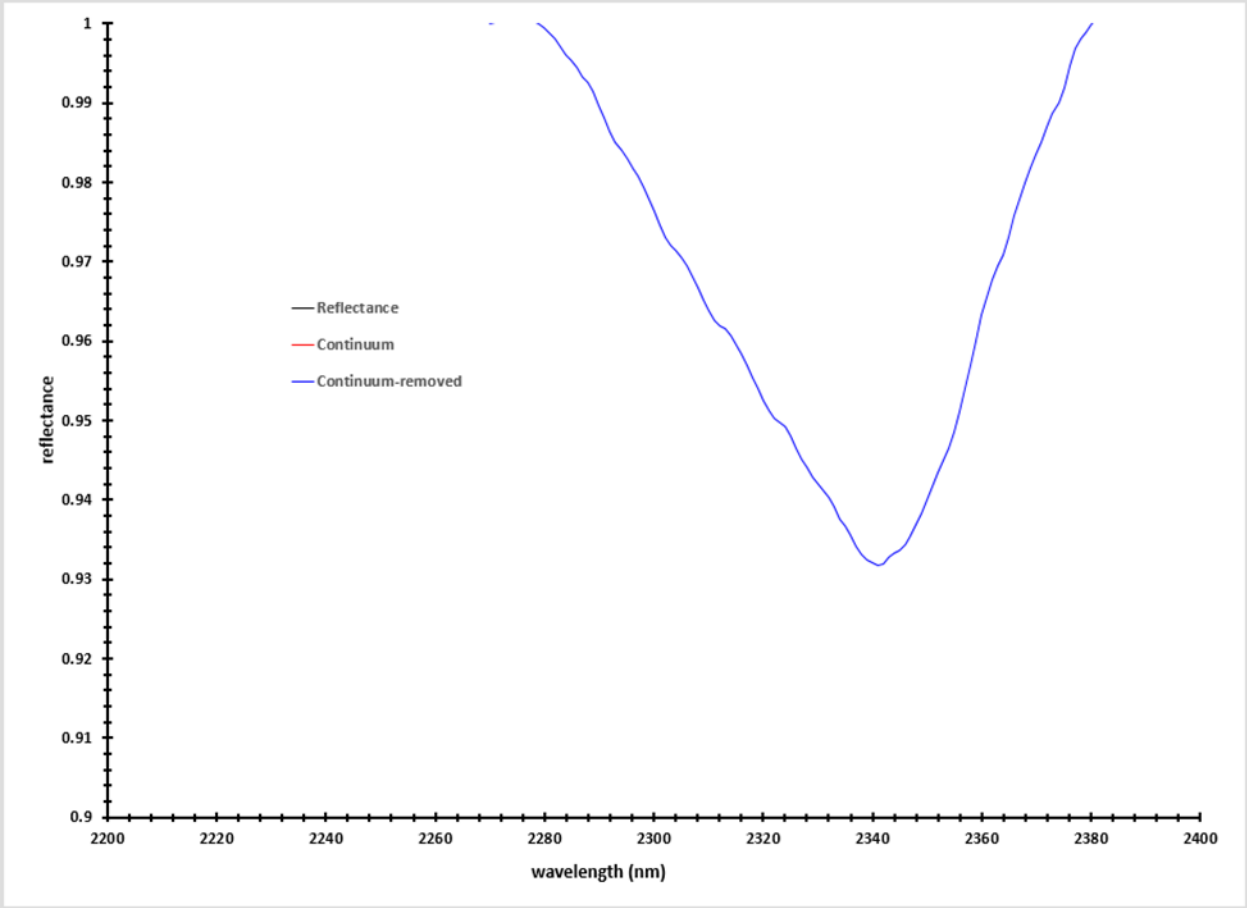

Figure 6: Continuum removed UTE001 spectrum showing a band centered at 2341 nm. The band shape indicates that this part of the sample is calcite dominated.

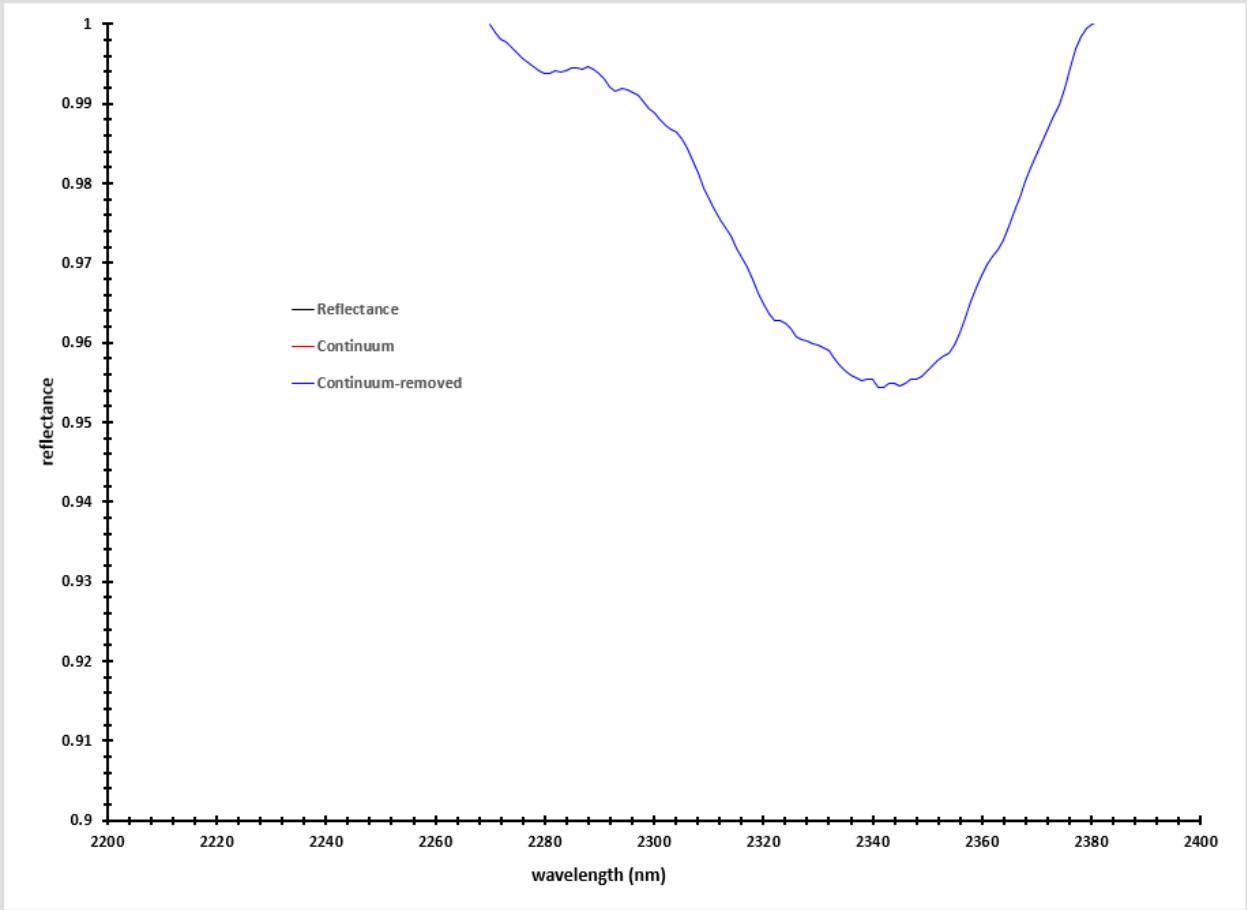

Figure 7: Continuum removed spectrum of UTE001 shows a band centered at 2344 nm. The band shape indicates that this part of the sample is a calcite/aragonite mixture.

Neither ferrihydrite nor goethite was detected in any of the data sets except for in the reflectance spectra, in which all reflectance spectra indicate the presence of either ferrihydrite or goethite by the absorption feature in the ~900 nm region (**Table 2**). The spectra show a general trend of being more ferrihydrite bearing, with often a mixture of the two minerals. Previous studies of carbonate-dominated spring sites have also found that the presence of low levels of iron oxyhydroxides is often only detectable using reflectance spectroscopy (e.g., Berard et al., 2013).

4.2 Raman spectroscopy

Phases identified in the Raman data are provided in **Table 2**. The Raman spectra consistently show peaks around ~1085 Δcm^{-1} for every sample, with minor peaks around ~710 – 730 Δcm^{-1} and

very faint peaks around ~180 – 280 Δcm^{-1} (**Figure 8a-d**). All these peaks are attributed to calcite, aragonite, or a mixture of both (Tomic et al., 2010; Parker et al., 2010; De La Pierre et al., 2014; Borromeo et al., 2018) and can be seen more prominently in some sample spectra versus others.

Table 2: Phases identified in the samples by reflectance spectroscopy, Raman spectroscopy, and X-ray diffractometry (XRD).

Sample Number	Phases identified by reflectance spectroscopy	Phases identified by Raman spectroscopy	Phases identified by X-ray diffractometry
UTE001	Ferrihydrite, Calcite/Aragonite, Silica	Calcite, Aragonite, Silica	Calcite, Aragonite, Quartz
UTE002	Ferrihydrite, Calcite/Aragonite, Silica	Calcite, Aragonite	Calcite, Aragonite, Quartz
UTE003	Goethite, Calcite/Aragonite	Calcite, Aragonite	Calcite, Aragonite
UTE004	Ferrihydrite, Calcite/Aragonite, Chlorophyll	Calcite, Aragonite, Silica	Calcite, Aragonite
UTE005	Goethite, Calcite/Aragonite, Silica	Calcite, Aragonite, Silica	Calcite, Aragonite, Quartz
UTE006	Ferrihydrite, Calcite/Aragonite, Chlorophyll	Calcite, Aragonite, Chlorophyll	Calcite, Aragonite
UTE007	Ferrihydrite, Calcite/Aragonite	Calcite, Aragonite	Calcite, Aragonite
UTE008	Ferrihydrite, Calcite/Aragonite	Calcite, Aragonite	Calcite, Aragonite
UTE009	Ferrihydrite/Goethite, Calcite/Aragonite, Chlorophyll	Calcite, Aragonite, Chlorophyll	Calcite, Aragonite
UTE010	Ferrihydrite/Goethite, Calcite/Aragonite, Chlorophyll, Silica	Calcite, Aragonite, Chlorophyll	Calcite, Aragonite, Quartz
UTE011	Ferrihydrite, Calcite/Aragonite, Chlorophyll	Calcite, Aragonite, Silica, Chlorophyll	Calcite, Aragonite

Table 3 provides a listing of Raman peaks corresponding to aragonite and calcite, as well as peak positions for the Crystal Geyser samples. Both calcite and aragonite show peaks in the range of 1080 – 1087 Δcm^{-1} and 698 – 712 Δcm^{-1}, making these peaks generally not differentiable between the two polymorphs. However, the faint peaks between ~180 – 280 Δcm^{-1} provide diagnostic information. Specifically, aragonite always has a peak around ~200 – 207 Δcm^{-1} whereas calcite always has a peak around ~273 – 282 Δcm^{-1} (Parker et al., 2010; Tomić et al., 2010; Borromeo et al., 2018). The Raman spectra for UTE002 and UTE007 show only aragonite present (**Figure 8a**), whereas the spectra for UTE003 and UTE004 show only calcite present for all spots analyzed

(**Figure 8b**). Samples such as UTE001 show mixtures of both aragonite and calcite present where one spot shows the presence of aragonite, and the other spot calcite (**Figure 8c**).

Table 3: Raman peak positions for calcite and aragonite from the literature compared with peaks identified in Utah Crystal Geyser samples.

Literature Values	**Peak Position (cm^{-1})**	**References**
Aragonite	1086, 707/702, 207, 154	Borromeo et al., 2018
Aragonite	1080, 698, 252, 200, 174, 147	Tomic et al., 2010
Aragonite	1087, 706/702, 206, 192, 181, 143	Parker et al., 2010
Calcite	1086, 712, 281, 154	Borromeo et al., 2018
Calcite	1084, 712, 282, 155	Tomic et al., 2010
Calcite	1087, 712, 281, 154	Parker et al., 2010
Sample Number	**Peak Position (cm^{-1})**	**Carbonate Phase Identified**
UTE001	1082, 702, 205, 154 and 710, 281, 205	Aragonite/Calcite
UTE002	1082, 710, 211, 146	Aragonite
UTE003	1082, 707, 279	Calcite
UTE004	1090, 707, 273, 148	Calcite
UTE005	1082, 699, 208, 157	Aragonite
UTE006	1085, 704, 208, 157	Aragonite
UTE007	1082, 702, 203, 148 and 702, 203	Aragonite
UTE008	1082, 710, 281, 203 and 699, 276, 205	Aragonite/Calcite
UTE009	1082, 704, 281	Calcite
UTE010	1082, 707, 273	Calcite
UTE011	1082, 702, 276	Calcite

Lastly, the XRF data confirmed the presence of silica in all the samples to varying extents. **Figure 8d** shows the Raman spectra of samples UTE001 and UTE011, which both show a peak around ~996 Δcm^{-1}, corresponding to silicon (Schmidt & Ziemann, 2000). The silica content is significantly higher in UTE001 than all other samples, therefore showing a prominent peak in the Raman spectra. The silica peak cannot be seen in the Raman spectra for the other samples except for UTE011, where it can be seen faintly (**Figure 8d**).

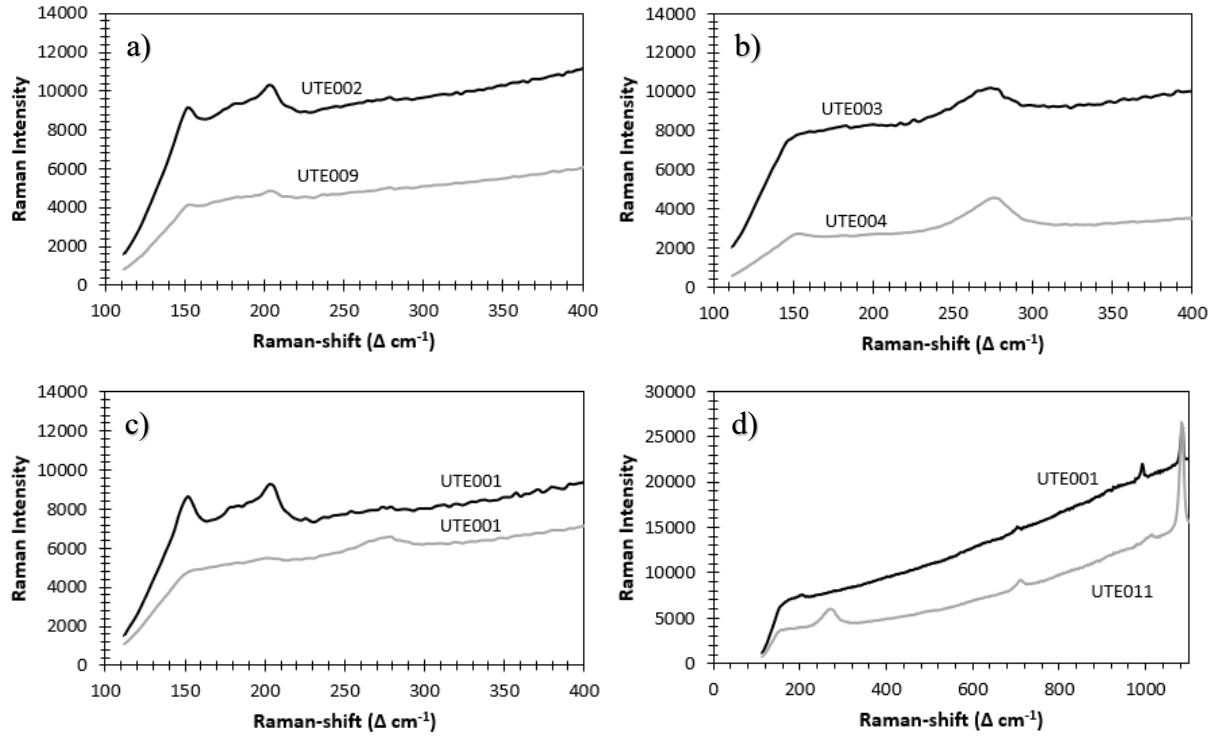

Figure 8: Raman spectra for (a) UTE002 and UTE007 show peaks corresponding to only aragonite for all spots analyzed. (b) UTE003 and UTE004 peaks correspond to only calcite for all spots analyzed. (c) UTE001 shows one peak for aragonite and a second peak for calcite, indicating that the Raman identified this as a likely mixture of both carbonates due to ongoing transformation. (d) UTE001 and UTE011 show peaks at ~996 Δcm^{-1}, which corresponds to silica. The spectra are uncorrected for the background continuum.

Organics, such as chlorophyll that were detected in reflectance spectra were also detected in the Raman spectra, despite strong fluorescence masking the Raman signal in many cases. **Figure 9** shows chlorophyll peaks are found near 3850 Δcm^{-1} (Das et al., 2005; Wolfe et al., 2006). Chlorophyll was visible in all the same Raman spectra in which it was visible in the reflectance spectra except for sample UTE004. The data for samples UTE006, UTE009, UTE010, and UTE011 showed the presence of organics in the Raman spectra.

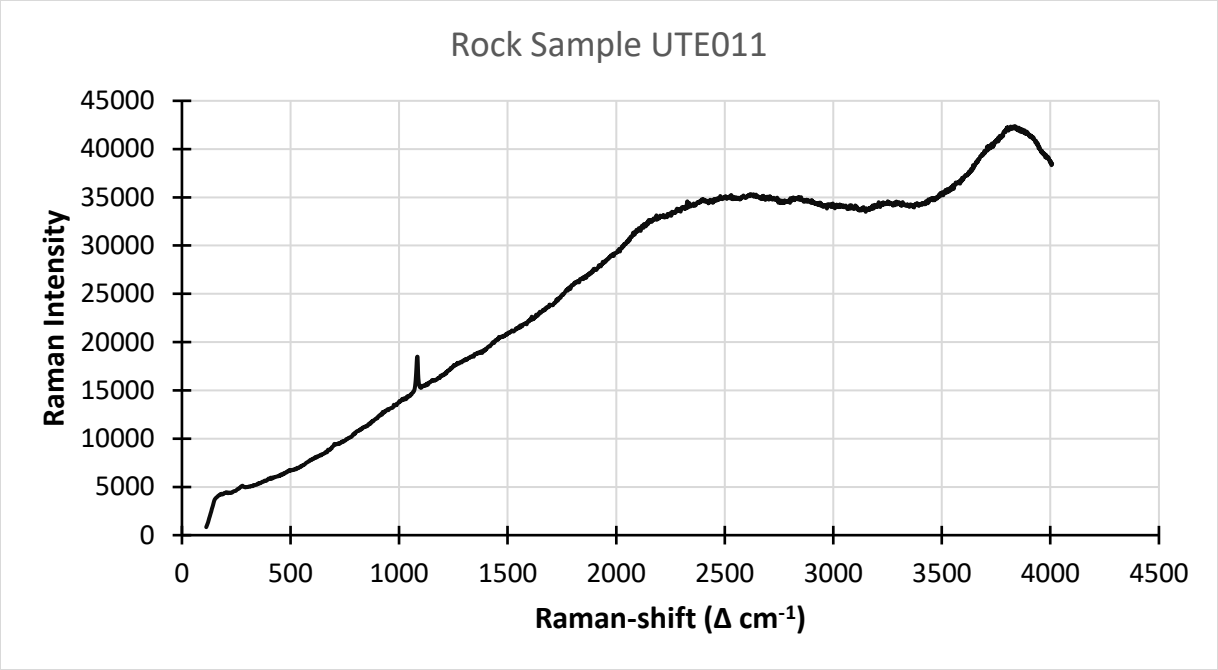

Figure 9: Raman spectra for sample UTE011 showing chlorophyll fluorescence "hump" around ~3850 Δcm^{-1}.

The effect of integration time and the visibility of low Raman-shift diagnostic peaks within the Raman spectra are evident (**Figure 10**). The top spectrum was run with an integration time of 1 ms, whereas the bottom spectrum was run with an integration time of 500 ms. The low Raman-shift diagnostic peaks are clear, and the noise is significantly reduced with interpretable peaks visible compared to the lower integration time.

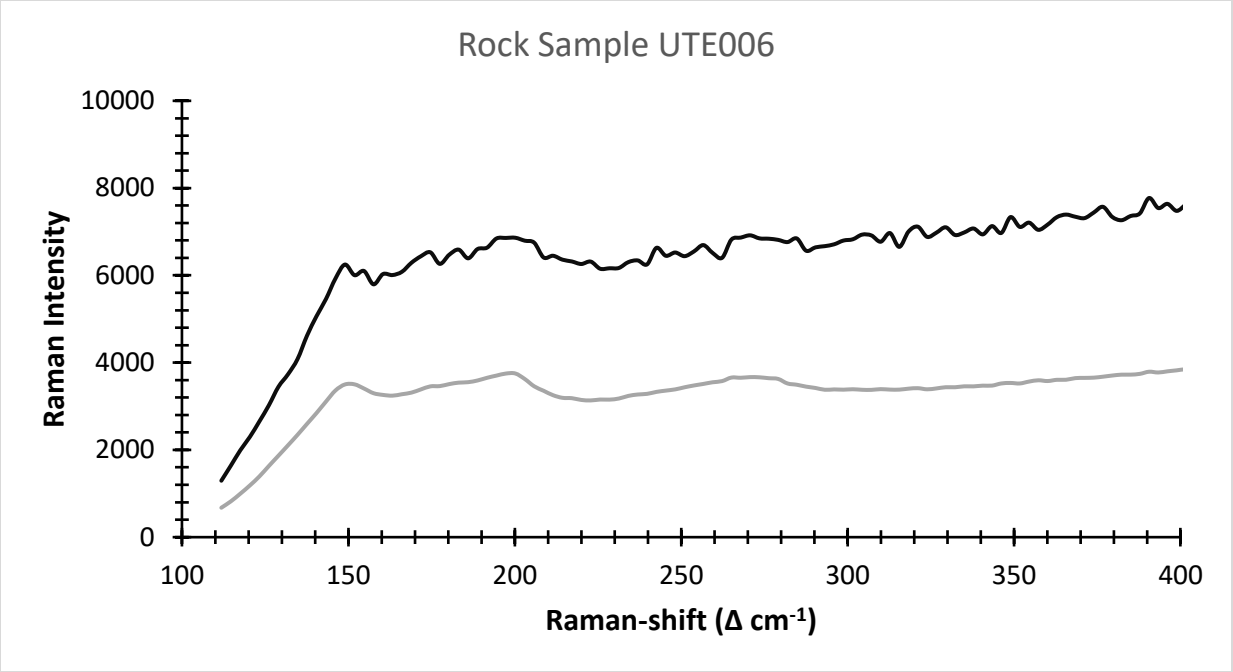

Figure 10: The top spectrum indicate data collected with a short integration time (1 ms), and the bottom spectrum is the same sample analyzed with a longer integration time (500 ms).

4.3 X-ray diffraction (XRD) and X-ray fluorescence (XRF)

Every sample collected from the site was analyzed with XRD to complement the Raman and reflectance data, and identified phases are also provided in **Table 2**. X-ray diffraction was useful in providing a "ground truth" interpretation of the phases identified in Raman and reflectance, but XRD analysis detection is generally limited to crystalline phases and phases with abundances of >∼1% (e.g., Berard et al., 2013; Cloutis et al., 2021; Stromberg et al., 2021). XRD showed calcite and aragonite as the major phases present in all samples. In addition, it showed that there was quartz present in samples UTE001, UTE002, UTE005, and UTE010. Quartz was identified in these samples by reflectance, but only two (UTE001 and UTE005) showed clear peaks due to quartz in the Raman spectra.

The XRD data confirmed some of the spectral identifications that were difficult to determine by reflectance (e.g., quartz). XRD was also able to detect minerals that were masked in Raman due to fluorescence, such as quartz. However, XRD was unable to detect the presence of chlorophyll, which was detected by reflectance. It was also unable to identify specific iron oxyhydroxides

which color many of the samples, likely due to some combination of low concentrations, low degree of crystallinity, or small grain size. Abundances of iron oxyhydroxides that are undetectable by XRD can impart a strong red color to carbonates (Berard et al., 2013).

X-ray fluorescence with wet chemistry results identified major and selected minor elements and are provided in **Table 4**. This information confirmed the presence of silicon which was seen in the reflectance spectra and some of the Raman spectra. The XRF data also show Sr present in each sample, ranging in concentration from approximately 6000 to 10,000 ppm.

Table 4: Compositional data for Utah Crystal Geyser samples conducted by Franklin and Marshall College.

Wt %	UTE 001	UTE 002	UTE 003	UTE 004	UTE 005	UTE 006	UTE 007	UTE 008	UTE 009	UTE 010	UTE 011
SiO_2	42.65	20.94	4.03	2.90	6.02	2.04	7.58	8.21	2.39	9.13	1.78
TiO_2	0.15	0.10	0.05	0.07	0.03	0.02	0.04	0.07	0.02	0.04	0.02
Al_2O_3	3.65	2.10	1.15	1.03	0.84	0.54	0.86	1.25	0.38	0.74	0.32
Fe_2O_3T[a]	1.44	2.38	8.05	1.03	12.38	1.16	0.78	1.69	9.13	1.29	1.39
MnO	0.13	0.22	0.17	0.15	0.12	0.18	0.22	0.16	0.16	0.18	0.18
MgO	1.71	1.17	0.62	0.85	0.36	0.42	2.30	1.37	0.40	1.94	0.40
CaO	47.46	71.09	80.91	91.50	77.79	93.29	86.09	84.87	84.95	84.80	93.63
Na_2O	0.92	0.76	0.21	0.89	0.77	0.77	0.72	1.15	0.78	0.64	0.67
K_2O	0.87	0.46	0.07	0.31	0.19	0.11	0.16	0.26	0.13	0.20	0.14
P_2O_5	0.07	0.04	0.09	0.02	0.13	0.01	0.02	0.03	0.13	0.02	0.01
SO_3	0.00	0.00	3.90	0.00	0.00	0.00	0.00	0.00	0.00	0.00	0.00
Cl	0.05	0.00	0.00	0.00	0.00	0.00	0.00	0.00	0.00	0.00	0.00
Total[b]	**99.10**	**99.26**	**95.35**	**98.75**	**98.63**	**98.54**	**98.77**	**99.06**	**98.47**	**98.98**	**98.54**
LOI[c]	29.28	37.04	40.69	42.27	40.47	43.17	41.90	41.22	41.28	40.42	41.13
FeO[d]	0.18	0.26	0.26	0.23	0.22	0.15	0.18	0.22	0.25	0.17	0.15
Fe_2O_3[e]	1.24	2.09	7.76	0.77	12.14	0.99	0.58	1.45	8.85	1.10	1.22
(ppm)											
Rb	42	<2	23	27	<2	<2	<2	<2	<2	<2	<2
Sr	7269	5887	8668	8654	9377	9929	8226	6556	9631	7631	9459
Zr	<2	<2	<2	<2	<2	<2	<2	<2	<2	<2	<2
Cr	<2	<2	<2	<2	<2	<2	<2	<2	<2	<2	<2
V	19	15	13	7	6	8	7	15	8	8	11
Ba	644	860	63	55	100	53	96	83	62	75	50

[a] All Fe expressed as Fe_2O_3.
[b] Total expressed on a volatile (LOI)- and Cl-free basis and with all Fe expressed as Fe_2O_3.
[c] LOI: loss on ignition; % weight loss after heating sample in air for 1 hour at 950° C.
[d] Wt.% FeO determined by wet chemistry.
[e] Wt.% Fe_2O_3 taken as the difference between total Fe and FeO.

4.4 Scanning Electron Microscopy (SEM)

Scanning electron microscopy provides fine-scale characterization of carbonates using backscattered electron imagery (BSE), which reveals internal structures such as preserved microbial fossils or structures associated with density and compositional variations. Using SEM imagery and elemental mapping can help to assess the biogenicity of carbonates.

The SEM was utilized in sample analysis analogous to how the PIXL instrument on the Perseverance rover is employed for sample analysis (Wade et al., 2016; Allwood et al., 2020). Backscattered electron images in **Figure 11** show finer-scale internal structures of samples UTE003 and UTE008. A cluster of ∼1 μm diameter aragonite crystals found in sample UTE003 are shown in **Figures 11a** and **11b**. **Figure 11c** is also from sample UTE003, showing crystals that are very different in structure and correspond to calcite with a few aragonite crystals in the mixture. This confirms that the sample is not homogeneous throughout and is a mixture of calcite and aragonite as indicated by the XRD results. **Figure 11d** is an electron image from sample UTE008 and shows a microbial community that has been preserved within the sample. The microbial fossils are circular in shape and are approximately 3 μm in diameter. **Figure 12** analyzes an individual microbial fossil with elemental maps showing the carbon and oxygen of the microbe encompassed within the calcium of the carbonate, confirming the ability of carbonates to entomb microbes and preserve them as fossils.

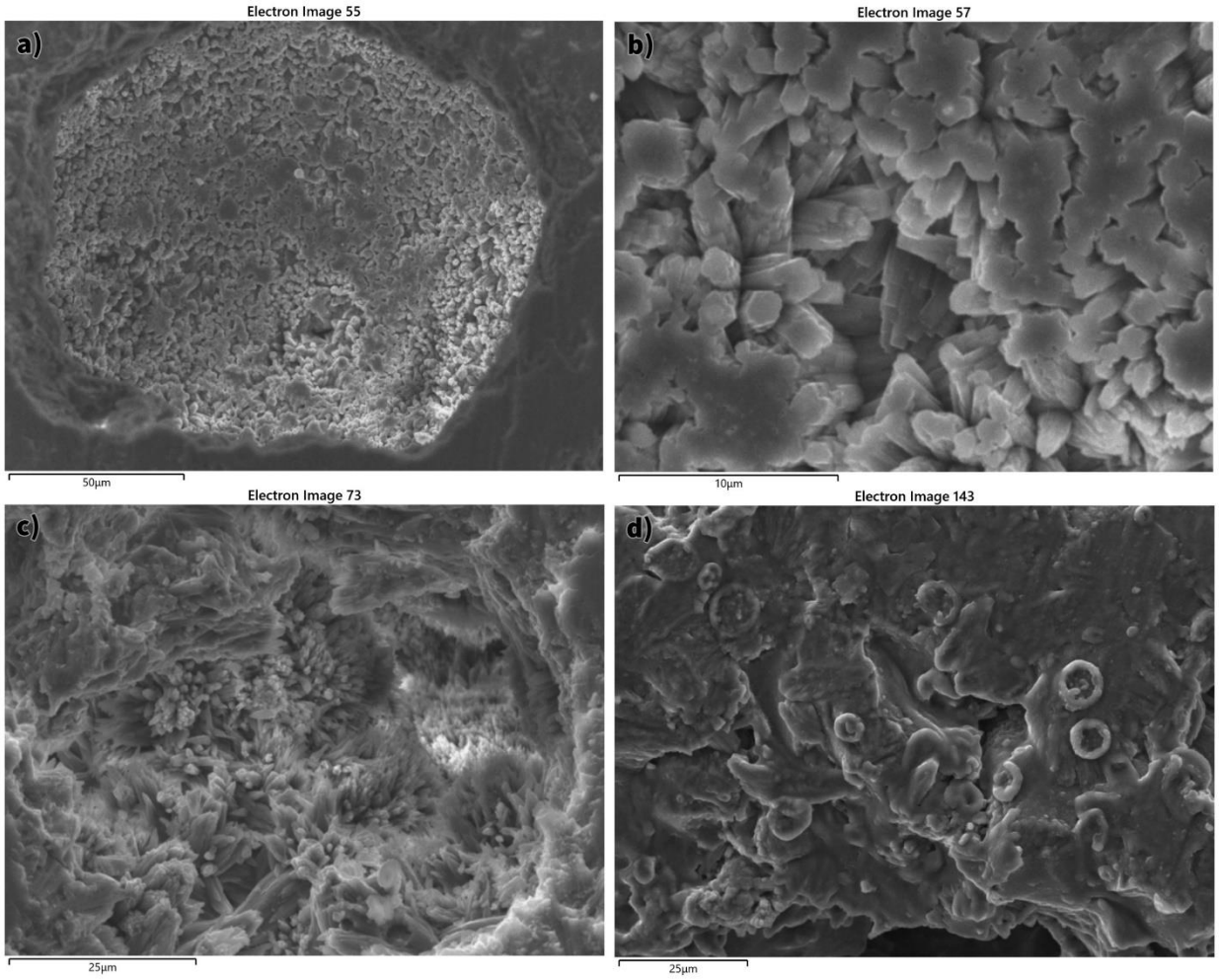

Figure 11: Scanning electron microscope backscattered (SEM-BSE) images. a) A patch of aragonite crystals (50 µm scale bar) from sample UTE003. b) The same aragonite crystals (10 µm scale bar). c) Calcite crystals (sharper pointed crystals) with a few embedded aragonite crystals, also from sample UTE003. d) A microbial community that has been preserved within the layers of the sample, found in sample UTE008. Microbe fossils appear as circular objects in the image.

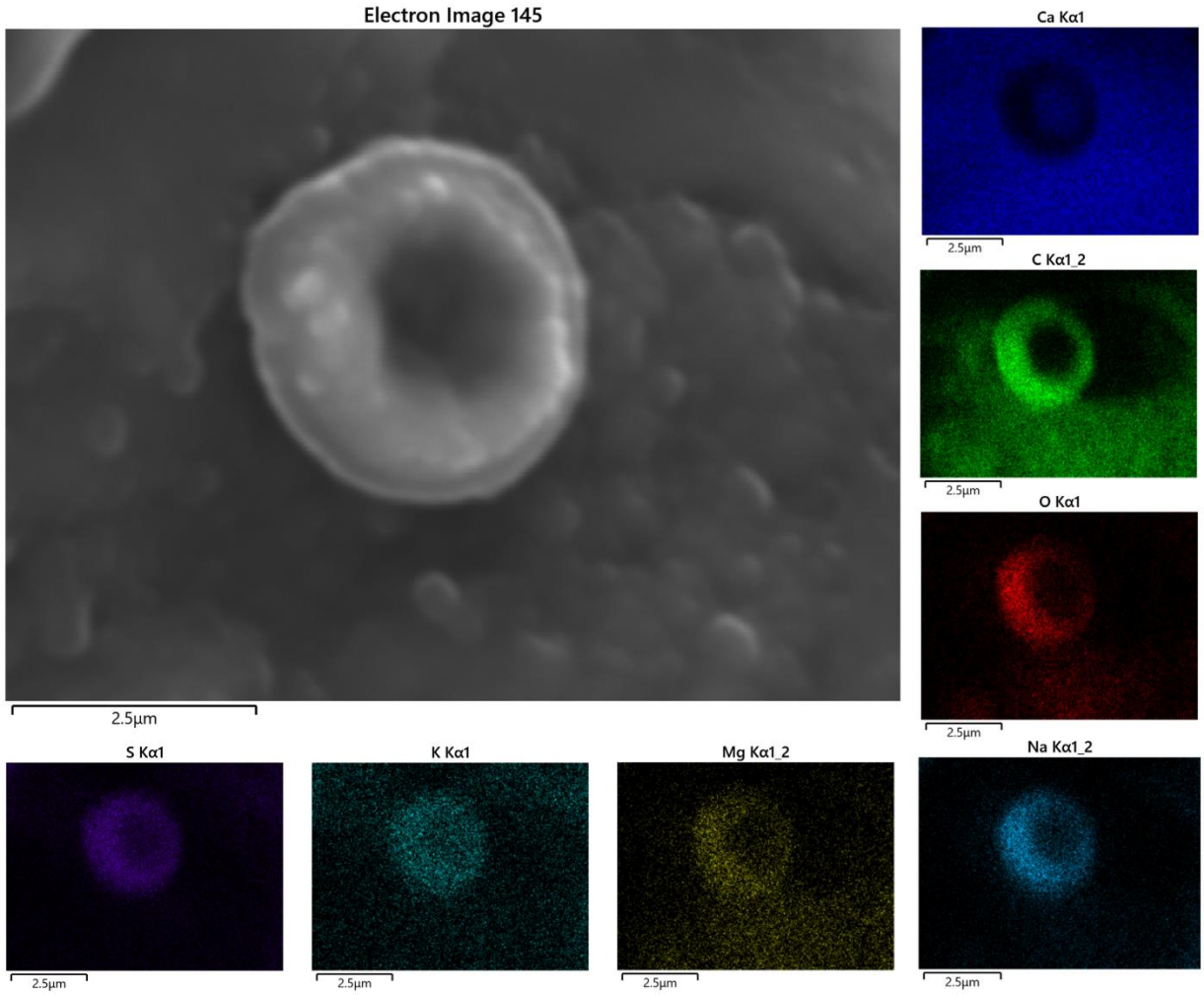

Figure 12: Individual microbe fossil approximately 3 µm in diameter embedded within the carbonate structure of the rock found in sample UTE008. Individual elemental maps show microbe fossil (low-Ca) is embedded within the carbonate structure (high-Ca).

Figure 13 shows a BSE image and elemental maps of calcium and iron for sample UTE003. The iron band (indicated in pink) shows the concentration of iron increased in one of the layers within the sample. **Figure 14** shows a BSE image of a polished interior surface of UTE005 perpendicular to its layering. Embedded within the layers are silicon clusters, as shown by the Si elemental map. This corresponds with the presence of quartz, as confirmed by XRD results.

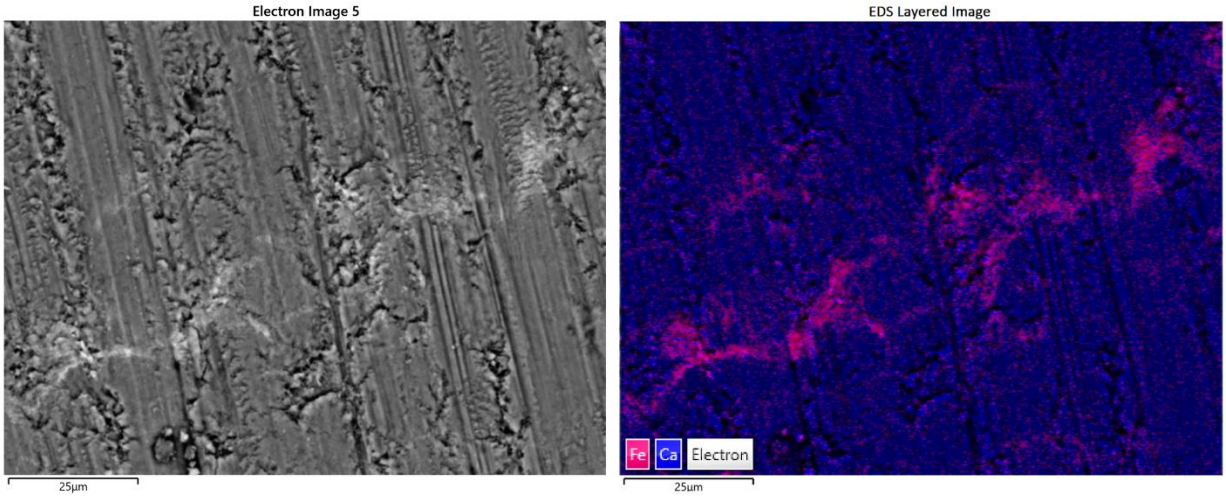

Figure 13: SEM-BSE image of a polished interior surface of UTE003 perpendicular to its layering showing a "vein" running approximately horizontally across the image. This vein can be seen in the iron and calcium map (indicated in blue) showing the iron (indicated in pink) concentration significantly higher, which is responsible for its appearance.

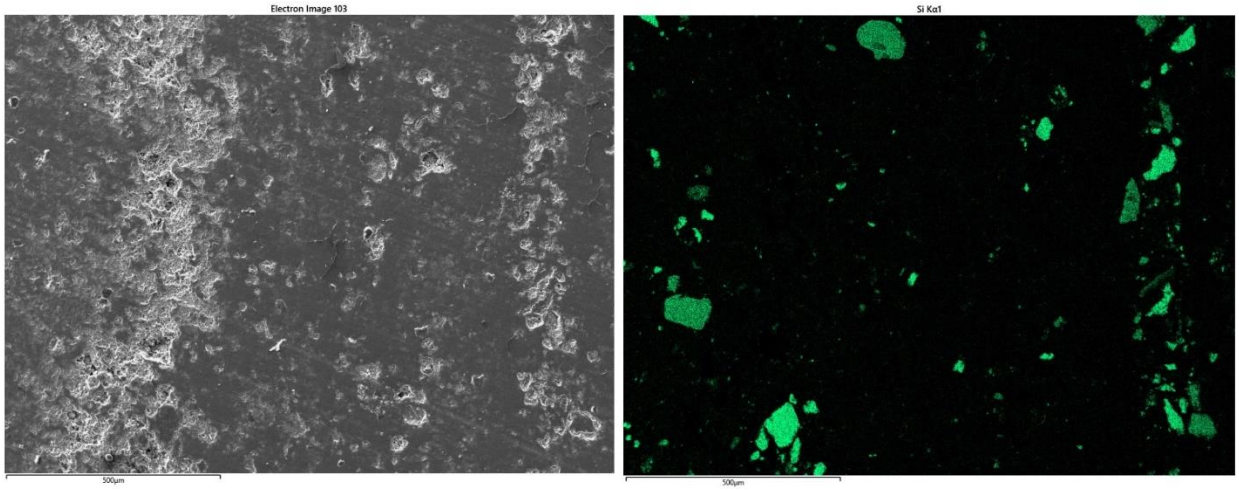

Figure 14: SEM-BSE image of a polished interior surface of UTE005 cut perpendicular to its layering. Embedded within the layers are silica clusters, as shown by the green elemental Si map.

4.5 Comparison of analytical techniques

Reflectance spectroscopy was able to identify the presence of carbonate minerals within the samples; however, it was not able to differentiate between pure calcite and calcite-dominated calcite+aragonite mixtures (**Table 2**). A continuum was calculated across the adsorption band at

~2340 nm (**Figures 6 & 7**), and the absorption band was compared to pure calcite and aragonite standards (**Figure 5**). In calcite and aragonite mixtures, aragonite is expressed as a more prominent shoulder at a shorter wavelength near 2300 nm (Craig, 2010). The continuum-removed absorption feature confirmed that the reflectance spectra are showing a mixture of the two carbonates based on the presence of the lower wavelength aragonite shoulder. The continuum-removed spectra can be used to roughly estimate the ratio of aragonite to calcite using band position, even though the mixture of the two does not shift the band position linearly (**Figure 5**) (Craig, 2010). Calcite dominates the spectrum unless aragonite is present in concentrations of >~70% (**Figure 5 and 15**) because the absorption coefficient of calcite at these wavelengths is much higher than that of aragonite (Craig, 2010). In **Figures 5 and 15**, a grain size of <45 μm was used to collect reflectance spectra from pure calcite to pure aragonite in increments of 10 wt. %. The band center for 100% calcite was 2336 nm and remained at 2336 nm until the mixture of aragonite reached 50%. However, even at 50% aragonite, the band center only shifted by 2 nm lower, to 2334 nm. At 80% aragonite, the band center shifted significantly lower to 2316 nm and finally to 2314 nm for 100% aragonite. Therefore, aragonite must be present at an abundance of at least 50 wt. % for there to be significant representation in the spectra.

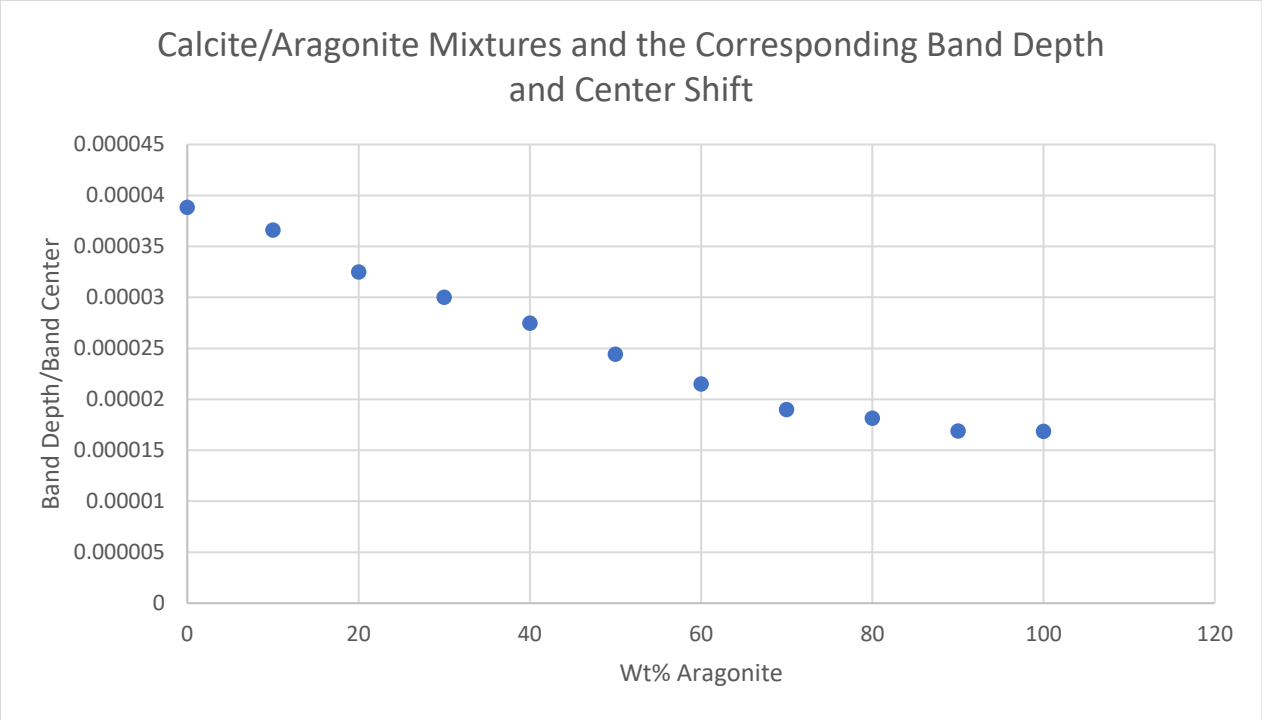

Figure 15: Band depth divided by band center for each increment of 10% increase of aragonite. Band depth decreases as aragonite increases, and band center lowers from 2336 nm to 2314 nm as aragonite increases (data collected by Craig, 2010).

Raman spectroscopy was able to distinguish between calcite and aragonite in the low wavenumber diagnostic peaks region (100 – 300 Δcm^{-1}) of the spectra. Our Raman analysis was based on single-point spectra and, therefore, might detect calcite in one spot and aragonite in another. Raman data for powdered samples (<45 µm) were able to detect calcite and aragonite at the same time based on their low wavenumber diagnostic peaks.

Reflectance and Raman spectroscopy were able to detect the presence of chlorophyll in a few of the samples at ~670 nm and ~3850 Δcm^{-1}, respectively. The faintness of this band and the complete lack of this band in other samples is likely due to the lack of microbes nearest to the geyser due to the high levels of the salinity of water from the geyser. Both reflectance and Raman spectroscopy were able to identify quartz in various samples, which were also confirmed by the XRD spectra.

The XRD identified calcite and aragonite in all samples. XRD was conducted on crushed and sieved samples <45 μm , creating a more representative sample of the present phases. Silica was present in all the samples according to XRF; however, XRD only indicated the presence of quartz in a few samples where the percentage of silica was higher.

Scanning electron microscopy with backscattered electron imaging was able to show microbial structures entombed within the carbonates confirming the preservation ability of carbonates (**Figures 11d & 10**). The SEM-BSE images also show fine layering where the concentration of iron is enhanced (**Figure 13**). The SEM-BSE imagery was also able to show areas of the same sample having aragonite crystals and another area having calcite crystals (**Figure 11a, b, c**). Thus, SEM-BSE is valuable for examining compositional and structural variations at submicron scales and determining mineralogy from crystal morphologies.

5.0 Discussion

5.1 Aragonite precipitation at Crystal Geyser

It is well understood that calcite is the most stable polymorph of calcium carbonate, and it has led to significant debate as to why metastable aragonite is precipitated in spring systems (e.g., McCauley & Roy 1974; Parker et al., 2010; Jones, 2017). While there have been many studies focused on calcite-aragonite precipitation, there has not been a universal factor attributed to controlling the precipitation of aragonite (Jones, 2017 and references therein). Aragonite precipitates preferentially from water with temperatures between 30 - 60°C (Lippmann, 1973; Folk, 1994; Pentecost, 2005). Crystal Geyser is significantly lower in temperature, at approximately 18°C (Potter-McIntyre, 2019). The presence of magnesium and strontium enhance the likelihood of aragonite precipitation (Malesani & Vannucchi, 1975; Loste et al., 2003; Pentecost, 2005; Jones & Renaut, 2010); however, the quantity of magnesium and strontium present in the Crystal Geyser samples is small but still significant enough that it may play a role in favor of aragonite over calcite precipitation (Pentecost, 2005). Research conducted by Lea (2003) shows that Sr^{2+} and Mg^{2+} substituting for Ca^{2+} in the carbonate structure is temperature dependant and can therefore be used in the field of palaeothermometry through which we can gain

information about the temperature of water in past climates. In addition, Mg/Ca rations in foraminifera calcite is also used as a palaeothermometer (Lea, 2003). Aragonite can easily accept strontium into its lattice due to the size of its crystallographic sites (Finch & Allison, 2007; Jones, 2017). A study by Salport et al. (2007) found that aragonite produced biogenically contained higher amounts of strontium and that strontium substitutes for calcium in the crystal lattice for biological precipitates. This could lead to a distorted crystal lattice resulting in an increase in the entropy and the stabilization energy and a decrease in the thermal resistance. Therefore, one of the minor contributing factors for aragonite precipitation at Crystal Geyser may be the presence of strontium.

The effect of temperature on calcium carbonate precipitation has been widely studied for all three polymorphs. A review by Jones (2017) reviewed relevant papers that analyzed the relationship between temperature and aragonite precipitation, and it was determined that temperatures over 30°C were generally required for aragonite precipitation. However, other studies have suggested that temperature does not control which polymorph is precipitated (Curl, 1962; Siegel & Reams, 1966; Hill & Forti, 1997). Despite the numerous studies that have tried to address this question, little attention has been given to aragonite precipitation below 30°C. There are examples of aragonite formed in lower temperatures ranging from 2.4 to 20°C, such as speleothems that are formed in caves (Hill & Forti, 1997). It was found that temperature is not a controlling factor for the formation of calcite and aragonite in caves of high latitudes, whereas caves in low latitudes require warmer temperatures (Hill & Forti, 1997). Despite these findings that temperature may not be a controlling factor for the formation of calcium carbonates, it may influence other variables such as reaction rates, ion availability, and diffusion rates (Curl, 1962).

Another factor supporting aragonite precipitation, irrespective of strontium content or temperature, is spring water with high CO_2 content and rapid CO_2 degassing. Several studies have found that supersaturation levels of CO_2 can determine the polymorph that will be precipitated (Jones, 2017). In scenarios where supersaturation is accompanied by rapid CO_2 degassing, aragonite is the favored polymorph (Holland et al., 1964). It was determined in a study by Holland et al. (1964) that rapid CO_2 degassing was a more important control in aragonite precipitation than magnesium content. Crystal Geyser is rich in CO_2, with eruptions occurring due to dissolved CO_2 in water

(Potter-McIntyre, 2019). Therefore, rapid CO_2 degassing with high CO_2 content is likely responsible for aragonite precipitation in this environment.

The role that pH plays in aragonite and calcite precipitation is poorly understood due to the number of parameters that affect carbonate precipitation (Jones, 2017). One study found that calcite precipitates at a pH > 11 and aragonite precipitates between pH 9.7 and 10.5 (Matsumoto et al., 2010), whereas a different study reported calcite precipitation with a pH > 12 and aragonite precipitation at pH = 11 (Tai & Chen, 1998). Crystal Geyser has a reported pH significantly lower, at 6.2 – 7 (Shipton et al., 2004; Potter-McIntyre et al., 2017), indicating that pH is not likely a factor supporting either aragonite or calcite precipitation at Crystal Geyser.

There is a large amount of research showing the presence of microbes and microbial mats affecting the precipitation of specific calcium carbonate polymorphs (Dupraz et al., 2009; Cangemi et al., 2016; Jones, 2017; Della Porta et al., 2022). All three polymorphs of calcium carbonate can form at around 20°C, approximately the same temperature as Crystal Geyser, in the presence of organic matter (Murray, 1954; Lowenstam & Weiner, 1983).

Crystal Geyser experience eruptions of the geyser every several hours and has a high deposition rate, which supports aragonite precipitation (Loste et al., 2003, and Jones and Renaut, 2010). This allows for the rapid entombment of microbes near the surface. Biofilms may allow for simultaneous precipitation of calcite and aragonite regardless of the aforementioned CO_2 degassing (Jones, 2017 and references therein). The erupted water also contains >200 μM dissolved Fe^{2+}, which is a known inhibitor of calcite formation (Cosmidis et al., 2001).

5.2 Age effects on carbonates at Crystal Geyser

The modern travertine deposit around the geyser is composed of a mixture of calcite and aragonite. A study by Barth and Chafetz (2015) determined that calcite is the predominant mineral composing the travertine; however, aragonite becomes more dominant near the vent. This is due to aragonite being precipitated first and transforming to calcite over time. In addition, Barth and Chafetz (2015)

found that red laminae always show calcite as the dominant mineral and yellow laminae show aragonite as the dominant mineral, but the reason for this was not explored.

As aragonite transforms into calcite, the external mode features weaken as the peak around 206 Δcm^{-1} disappears and a peak around 281 Δcm^{-1} appears, showing the transformation to calcite is complete. The relative proportion of aragonite to calcite can be estimated from the ratio of these two peaks (Edwards et al., 2005; Parker et al., 2010). The Raman spectra for UTE002 and UTE007 show only aragonite present (**Figure 8a**), whereas the spectra for UTE003 and UTE004 show only calcite present for all spots analyzed (**Figure 8b**). However, as the entire sample is not transforming uniformly throughout, there can be mixtures of both aragonite and calcite present, as is the case with UTE001, where one spot shows the presence of aragonite, and the other spot calcite (**Figure 8c**).

In addition to aragonite transforming to calcite with age, the iron oxyhydroxides present in the samples will also transform with age. Ferrihydrite is the youngest iron oxyhydroxide present and is expected to precipitate first and is seen in the reflectance spectra. **Figure 4b** shows ferrihydrite in the spectrum for UTE007, with goethite contributing to the spectrum of sample UTE009 (Arnold, 2007). Ferrihydrite will transform to goethite, and then hematite, and the timescale of this transformation depends largely on the temperature. At low temperatures, it can take several years, whereas it can only take 10 minutes at high temperatures, around 92°C (Das et al., 2011).

The presence of iron oxyhydroxides is only determinable from the reflectance spectra in the 900 nm region and not in the XRD or Raman spectra. The reflectance spectra show a stronger presence of ferrihydrite than goethite, with no hematite being detected. This indicates that the age of these samples is relatively young.

6.0 Low- versus high-temperature calcium carbonates

Carbonates of low-temperature origin are commonly heterogeneous, as detected with reflectance and Raman spectroscopy of the Crystal Geyser samples, which showed both calcite and aragonite

throughout each sample. As carbonate transformation is inhibited at lower temperatures, minerals do not homogenize easily, nor do they transform quickly (Jones, 2017).

Spectrally, carbonates that are of low-temperature origin such as those found at Crystal Geyser are no different from those of high-temperature origin when analyzed with reflectance or Raman spectroscopy. However, since temperature affects the crystal formation in terms of grain size and morphology, differences may be visible only in microscopic images. While much information can be gained from the spectroscopic techniques used in this study, definitive differentiation between hydrothermal and low-temperature carbonates cannot be made using spectroscopic techniques alone. Other data sources, such as geomorphology, may be required. In addition, isotope chemistry using thermometry is the best way to determine the temperature origin of a carbonate (Halevy et al., 2011). Cathodoluminescence by scanning electron microscopy or laser-induced fluorescence may also be able to discern the mechanism of formation (Toffolo et al., 2019).

7.0 Implications for extraterrestrial carbonates

Although there is much debate about the temperature at which the carbonates on Martian meteorite ALH 84001 formed, a study by Halevy et al. (2011) suggests that they formed around 18°C temperatures identical to Crystal Geyser. A study by Lee et al. (2014) analyzed 14 carbonaceous chondrite meteorites from CM2.5 to CM2.0, and all were found to contain calcite, with aragonite occurring in the CM2.5 to CM2.2 meteorites. Aragonite was the first carbonate to precipitate in the meteorites and grew from magnesium-rich solutions. In the least altered of these meteorites, the aragonite crystals formed in clusters owing to the physical restriction of aqueous fluids within the low permeability matrix.

The known presence of calcium carbonates on Ceres (Carrozzo et al., 2018) may be informed by the results from Crystal Geyser. While the temperature of any erupting materials is poorly constrained, once on the surface, they will undergo rapid cooling and, if driven by CO_2-charged fluids, also undergo rapid CO_2 degassing. Mg-Ca carbonates, such as calcite, magnesite, and dolomite, have been detected across the surface of Ceres (Carrozzo et al., 2018; Palomba et al., 2019).

Kaplan et al. (2020) were able to identify calcite within the carbonate veins on Bennu, however, they were unable to determine the presence of aragonite due to how similar their spectral properties and the spectral resolution of the OVIRS data. They were able to determine that approximately 64% of the carbonate signatures detected on Bennus' Nightingale crater sample site are consistent with calcite which indicates a strong potential for the presence of aragonite (Kaplan et al., 2020).

This study reiterates the value of Raman and reflectance spectroscopy in determining mineralogy, which are two common techniques used by the Mars Curiosity and Perseverance rovers (Mandon et al., 2023). The interior of Jezero crater has mineralogical diversity, with the Marginal fractured unit having strong carbonate signatures of Fe/mg-carbonates (Mandon et al., 2023). Carbonate signatures have also been detected within the Máaz and Séítah formations. The use of VISIR reflectance spectroscopy by SuperCam has been found to be sensitive to carbonate detections thus far with detections increasing moving towards the Marginal unit and into the Upper Fan (Mandon et al., 2023). The combination of using both visible and near-infrared allow for high sensitivity in detecting Fe-rich minerals, including carbonates (Mandon et al., 2023). This study will support further carbonate detections on Mars, specifically Ca-carbonate detection, and will allow for the spectral interpretation of metastable aragonite.

Raman and reflectance spectroscopy are useful for the detection of organics such as Chlorophyll and could be useful in the detection of organics in Solar System bodies. Chlorophyll was visible in all the same Raman spectra in which it was visible in the reflectance spectra except for sample UTE004. Sample UTE006, UTE009, UTE010, and UTE011 showed the presence of organics in the Raman spectra. This indicates that despite the large fluorescence hump in the Raman data, not all organic signals are masked, and that Raman could be used for the detection of organics.

8.0 Summary and Conclusions

Crystal Geyser is a unique site for understanding the non-hydrothermal, CO_2-charged eruption of subsurface water. Spectroscopic analysis using reflectance and Raman spectroscopy, and XRD determined that precipitates at the site are composed predominantly of aragonite and calcite. The reflectance spectra were able to show the presence of a mixture of calcite and aragonite and

approximate the ratio of calcite to aragonite present. Raman spectroscopy was able to differentiate between the two using low Raman-shift diagnostic peaks. The SEM provided electron images showing the different crystal shapes of aragonite and calcite. The XRF indicated the precipitates are rich in Sr and poor in Mg and that Sr can be readily accepted into the aragonite lattice. It was also determined that temperature has no impact on aragonite precipitation at this locality and that CO_2 supersaturation and degassing is the key factor supporting the precipitation of aragonite and calcite. This novel site can inform our understanding and exploration of carbonate deposits on many planetary surfaces.

SEM analysis of the samples indicates that microbial fossils can be entombed at such sites and could be detectable on the basis of both preserved morphologies and composition. This study has implications for how low-temperature calcium carbonate-bearing sites on Mars could be explored and recognized, the relative strengths and weaknesses of different analytical instruments on Mars rovers, as well as for how various techniques would be applicable to the analysis of such samples from Mars.

In terms of icy moons and asteroids, our results indicate that aragonite-calcite end member abundances could be constrained from remote sensing data using reflectance spectroscopy. The low-temperature, rapid degassing nature of Crystal Geyser may provide a more suitable analogue for understanding any carbonate deposits on icy moons than higher-temperature hydrothermal deposits.

9.0 Acknowledgements

This study was supported by the Canadian Space Agency (grant 22 EXPCO14), the Natural Sciences and Engineering Research Council of Canada (grants RGPIN-2021-02995 and RTI-2020-00157), the Canada Foundation for Innovation, and the Manitoba Research Innovation Fund (grant #CFI 1504), and the University of Winnipeg. Mertzman thanks the NSF-MRI Program for XRF Instrumentation support (NSF- EAR 1872311) and Karen R. Mertzman for her ongoing meticulous work in the lab.

10.0 References

Allen, C. C., & Oehler, D. Z. (2008). A case for ancient springs in Arabia Terra, Mars. Astrobiology, 8(6), 1093–1112. https://doi.org/10.1089/ast.2008.0239

Allender, E. J., Cousins, C. R., Gunn, M. D., & Mare, E. R. (2021). Multiscale spectral discrimination of poorly crystalline and intermixed alteration phases using aerial and ground-based ExoMars rover emulator data. Icarus, 367, 114541. https://doi.org/10.1016/j.icarus.2021.114541

Allwood, A. C., Wade, L. A., Foote, M. C., Elam, W. T., Hurowitz, J. A., Battel, S., Dawson, D. E., Denise, R. W., Ek, E. M., Gilbert, M. S., King, M. E., Liebe, C. C., Parker, T., Pedersen, D. A. K., Randall, D. P., Sharrow, R. F., Sondheim, M. E., Allen, G., Arnett, K., … Zimmerman, R. (2020). PIXL: Planetary Instrument for X-Ray Lithochemistry. Space Science Reviews, 216(8), 134. https://doi.org/10.1007/s11214-020-00767-7

Arnold, L. (2007). Earthshine observation of vegetation and implication for life detection on other planets—A review of 2001—2006 works. Space Science Reviews, 135. https://doi.org/10.1007/s11214-007-9281-4

Baer, J. L. & Rigby, J. K. (1978) Geology of the Crystal geyser and environmental implications of its effluent, Grand Country, Utah. *Utah Geol.*, **5**, 125-130.

Barth, J. A., & Chafetz, H. S. (2015). Cool water geyser travertine: Crystal Geyser, Utah, USA. Sedimentology, 62(3), 607–620. https://doi.org/10.1111/sed.12158

Beegle, L., Bhartia, R., White, M., DeFlores, L., Abbey, W., Wu, Y.-H., Cameron, B., Moore, J., Fries, M., Burton, A., Edgett, K. S., Ravine, M. A., Hug, W., Reid, R., Nelson, T., Clegg, S., Wiens, R., Asher, S., & Sobron, P. (2015). SHERLOC: Scanning habitable environments with Raman amp; luminescence for organics amp; chemicals. 2015 IEEE Aerospace Conference, 1–11. https://doi.org/10.1109/AERO.2015.7119105

Bell III, J. F., Godber, A., McNair, S., Caplinger, M. A., Maki, J. N., Lemmon, M. T., Van Beek, J., Malin, M. C., Wellington, D., Kinch, K. M., Madsen, M. B., Hardgrove, C., Ravine, M. A., Jensen, E., Harker, D., Anderson, R. B., Herkenhoff, K. E., Morris, R. V., Cisneros, E., & Deen, R. G. (2017). The Mars Science Laboratory Curiosity rover Mastcam instruments: Preflight and in-flight calibration, validation, and data archiving. Earth and Space Science, 4(7), 396–452. https://doi.org/10.1002/2016EA000219

Bell, J. F., Maki, J. N., Mehall, G. L., Ravine, M. A., Caplinger, M. A., Bailey, Z. J., Brylow, S., Schaffner, J. A., Kinch, K. M., Madsen, M. B., Winhold, A., Hayes, A. G., Corlies, P., Tate, C., Barrington, M., Cisneros, E., Jensen, E., Paris, K., Crawford, K., … Wolff, M. J. (2021). The Mars 2020 Perseverance Rover Mast Camera Zoom (Mastcam-Z) Multispectral, stereoscopic imaging investigation. Space Science Reviews, 217(1), 24. https://doi.org/10.1007/s11214-020-00755-x

Bennett, K., Fox, V., Bryk, A., Dietrich, W., Fedo, C., Edgar, L., Thorpe, M., Williams, A., Wong, G., Dehouck, E., Mcadam, A., Sutter, B., Millan, M., Banham, S., Bedford, C., Bristow, T., Fraeman, A., Vasavada, A., Grotzinger, J., & Caravaca, G. (2022). The Curiosity Rover's Exploration of Glen Torridon, Gale Crater, Mars: An Overview of the Campaign and Scientific Results. Journal of Geophysical Research: Planets, 128. https://doi.org/10.1029/2022JE007185

Berard, G., D. Applin, E. Cloutis, J. Stromberg, R. Sharma, P. Mann, S. Grasby, R. Bezys, B. Horgan, K. Londry, M. Rice, B. Last, F. Last, P. Badiou, G. Goldsborough, and J.F. Bell III (2013) A hypersaline spring analogue in Manitoba, Canada for ancient spring deposits on Mars. Icarus 224, 399-412.

Beruto, D., & Giordani, M. (1993). Calcite and aragonite formation from aqueous calcium hydrogencarbonate solutions: Effect of induced electromagnetic field on the activity of CaCO3 nuclei precursors. Journal of the Chemical Society, Faraday Transactions, 89(14), 2457–2461. https://doi.org/10.1039/FT9938902457

Bhartia, R., Beegle, L. W., DeFlores, L., Abbey, W., Razzell Hollis, J., Uckert, K., Monacelli, B., Edgett, K. S., Kennedy, M. R., Sylvia, M., Aldrich, D., Anderson, M., Asher, S. A., Bailey, Z., Boyd, K., Burton, A. S., Caffrey, M., Calaway, M. J., Calvet, R., … Zan, J. (2021). Perseverance's Scanning Habitable Environments with Raman and Luminescence for Organics and Chemicals (SHERLOC) Investigation. Space Science Reviews, 217(4), 58. https://doi.org/10.1007/s11214-021-00812-z

Blake, D., Vaniman, D., Achilles, C., Anderson, R., Bish, D., Bristow, T., Chen, C., Chipera, S., Crisp, J., Des Marais, D., Downs, R. T., Farmer, J., Feldman, S., Fonda, M., Gailhanou, M., Ma, H., Ming, D. W., Morris, R. V., Sarrazin, P., … Yen, A. (2012). Characterization and calibration of the CheMin mineralogical instrument on Mars Science Laboratory. Space Science Reviews, 170(1), 341–399. https://doi.org/10.1007/s11214-012-9905-1

Borg, L. E., Connelly, J. N., Nyquist, L. E., Shih, C. Y., Wiesmann, H., & Reese, Y. (1999). The age of the carbonates in martian meteorite ALH84001. Science (New York, N.Y.), 286(5437), 90–94. https://doi.org/10.1126/science.286.5437.90

Borromeo, L., Egeland, N., Wetrhus Minde, M., Zimmermann, U., Andò, S., Madland, M. V., & Korsnes, R. I. (2018). Quick, easy, and economic mineralogical studies of flooded chalk for EOR experiments using Raman spectroscopy. Minerals, 8(6), 221. https://doi.org/10.3390/min8060221

Boynton, W. V., Ming, D. W., Kounaves, S. P., Young, S. M. M., Arvidson, R. E., Hecht, M. H., Hoffman, J., Niles, P. B., Hamara, D. K., Quinn, R. C., Smith, P. H., Sutter, B., Catling, D. C., & Morris, R. V. (2009). Evidence for calcium carbonate at the Mars Phoenix landing site. Science, 325(5936), 61–64. https://doi.org/10.1126/science.1172768

Bramble, M. S., Mustard, J. F., & Salvatore, M. R. (2017). The geological history of Northeast Syrtis Major, Mars. Icarus, 293, 66–93. https://doi.org/10.1016/j.icarus.2017.03.030

Bridges, J. C., Hicks, L. J., & Treiman, A. H. (2019). Chapter 5—Carbonates on Mars. In J. Filiberto & S. P. Schwenzer (Eds.), Volatiles in the Martian crust (pp. 89–118). Elsevier. https://doi.org/10.1016/B978-0-12-804191-8.00005-2

Brown, W. H., Fyfe, W. S., & Turner, F. J. (1962). Aragonite in California glaucophane schists, and the kinetics of the aragonite—calcite transformation. Journal of Petrology, 3(3), 566–582. https://doi.org/10.1093/petrology/3.3.566

Bultel, B., Viennet, J.-C., Poulet, F., Carter, J., & Werner, S. (2019). Detection of carbonates in Martian weathering profiles. Journal of Geophysical Research. Planets, 124(4), 989–1007. https://doi.org/10.1029/2018JE005845

Burnside, N.M. (2010) *U-Th dating of travertines on the Colorado Plateau: implications for the leakage of geologically stored CO_2* [Doctoral Dissertation, University of Glasgow].

Buz, J., Ehlmann, B. L., Maki, J., Kinch, K., Madsen, M. B., Johnson, J. R., Rice, M. S., & Bell, J. F. (2019). Photometric characterization of lucideon and avian technologies color standards including application for calibration of the mastcam-z instrument on the mars 2020 rover. Optical Engineering, 58(2). https://doi.org/10.1117/1.OE.58.2.027108

Cady, S. L., & Farmer, J. D. (1996). Fossilization processes in siliceous thermal springs: trends in preservation along thermal gradients. In G. R. Bock & J. A. Goode (Eds.), Novartis Foundation Symposia (pp. 150–173). John Wiley & Sons, Ltd. https://doi.org/10.1002/9780470514986.ch9

Cady, S. L., Farmer, J. D., Grotzinger, J. P., Schopf, J. W., & Steele, A. (2003). Morphological biosignatures and the search for life on Mars. Astrobiology, 3(2), 351–368. https://doi.org/10.1089/153110703769016442

Campbell, J. L., Thomson, D. D., Flannigan, E. L., Holmes, N. G., Tesselaar, D. W., & VanBommel, S. (2019). A re-examination of the fundamental parameters approach to

calibration of the Curiosity rover alpha particle X-ray spectrometer. Nuclear Instruments and Methods in Physics Research Section B: Beam Interactions with Materials and Atoms, 447, 22–29. https://doi.org/10.1016/j.nimb.2019.03.036

Canet, C., María Prol-Ledesma, R., Melgarejo, J.-C., & Reyes, A. (2003). Methane-related carbonates formed at submarine hydrothermal springs: A new setting for microbially-derived carbonates? Marine Geology, 199(3), 245–261. https://doi.org/10.1016/S0025-3227(03)00193-2

Cangemi, M., Censi, P., Reimer, A., D'Alessandro, W., Hause-Reitner, D., Madonia, P., Oliveri, Y., Pecoraino, G., & Reitner, J. (2016). Carbonate precipitation in the alkaline lake Specchio di Venere (Pantelleria Island, Italy) and the possible role of microbial mats. Applied Geochemistry, 67, 168–176. https://doi.org/10.1016/j.apgeochem.2016.02.012

Cardoso, S. S. S., Cartwright, J. H. E., & Sainz-Díaz, C. I. (2018). Carbonate-hydroxide chemical-garden tubes in the soda ocean of Enceladus: Abiotic membranes and microtubular forms of calcium carbonate. Icarus, 319, 337–348. https://doi.org/10.1016/j.icarus.2018.09.020

Carr, M. H., Belton, M. J. S., Chapman, C. R., Davies, M. E., Geissler, P., Greenberg, R., McEwen, A. S., Tufts, B. R., Greeley, R., Sullivan, R., Head, J. W., Pappalardo, R. T., Klaasen, K. P., Johnson, T. V., Kaufman, J., Senske, D., Moore, J., Neukum, G., Schubert, G., … Veverka, J. (1998). Evidence for a subsurface ocean on Europa. Nature, 391(6665), 363–365. https://doi.org/10.1038/34857

Carrozzo, F. G., De Sanctis, M. C., Raponi, A., Ammannito, E., Castillo-Rogez, J., Ehlmann, B. L., Marchi, S., Stein, N., Ciarniello, M., Tosi, F., Capaccioni, F., Capria, M. T., Fonte, S., Formisano, M., Frigeri, A., Giardino, M., Longobardo, A., Magni, G., Palomba, E., … Russell, C. T. (2018). Nature, formation, and distribution of carbonates on Ceres. Science Advances, 4(3), e1701645. https://doi.org/10.1126/sciadv.1701645

Carter, J. and Poulet, F., 2012. Orbital identification of clays and carbonates in Gusev crater. Icarus, 219(1), pp.250-253

Casella, L. A., Griesshaber, E., Yin, X., Ziegler, A., Mavromatis, V., Müller, D., Ritter, A.-C., Hippler, D., Harper, E. M., Dietzel, M., Immenhauser, A., Schöne, B. R., Angiolini, L., & Schmahl, W. W. (2017). Experimental diagenesis: Insights into aragonite to calcite transformation of Arctica islandica shells by hydrothermal treatment. Biogeosciences, 14(6), 1461–1492. https://doi.org/10.5194/bg-14-1461-2017

Clark, R. N., & Roush, T. L. (1984). Reflectance spectroscopy: Quantitative analysis techniques for remote sensing applications. Journal of Geophysical Research: Solid Earth, 89(B7), 6329–6340. https://doi.org/10.1029/JB089iB07p06329

Cloutis, E., McCraig, M., Mustard, J., Kruzelecky, R., Jamroz, W., Scott, A., Bish, D., Poulet, F., Bibring, J.-P., & King, P. (2007). Stability of hydrated minerals on Mars. Geophys. Res. Lett, 34, L20202. https://doi.org/10.1029/2007GL031267

Cloutis, E., Mccormack, K., Belliii, J., Hendrix, A., Bailey, D., Craig, M., Mertzman, S., Robinson, M., & Riner, M. (2008). Ultraviolet spectral reflectance properties of common planetary minerals. Icarus, 197(1), 321–347. https://doi.org/10.1016/j.icarus.2008.04.018

Cloutis, E., J. Stromberg, D. Applin, S. Connell, K. Kubanek, J. Kuik, A. Lechowicz, A. Parkinson, M. Ramirez, N. Turenne, J. Cieszecki, M. Germinario, R. Kum, R. Parson, R. Walker, E. Wiens, J. Wiens, and S. Mertzman (2021) The Lake St. Martin impact structure (Manitoba, Canada): A simulated rover exploration of a sulfate-bearing impact crater. Planetary and Space Science, 208, 105336; https://doi.org/10.1016/j.pss.2021.105336.

Cosmidis, J., O'Reilly, S., Ellison, E. T., Crispin, K. L., Diercks, D., & Templeton, A. S. (2021). Carbonate polymorphism controlled by microbial iron redox dynamics at a natural CO_2 leakage site (Crystal Geyser, Utah). https://eartharxiv.org/repository/view/2523/

Craig, M. A. (2010). *The Effects of Impact on the NIR Spectra of Carbonates and Calibrations for Use in Planetary Remote Sensing* [Master's thesis, The University of Winnipeg].

Curl, R. L. (1962). The aragonite-calcite problem.

Das, B., Vinebrooke, R., Sanchez-Azofeifa, G. A., Rivard, B., & Wolfe, A. (2005). Inferring sedimentary chlorophyll concentrations with reflectance spectroscopy: A novel approach to reconstructing historical changes in the trophic status of mountain lakes. Canadian Journal of Fisheries and Aquatic Sciences, 62, 1067–1078. https://doi.org/10.1139/f05-016

Das, S., Hendry, M. J., & Essilfie-Dughan, J. (2011). Transformation of two-line ferrihydrite to goethite and hematite as a function of pH and temperature. Environmental Science & Technology, 45(1), 268–275. https://doi.org/10.1021/es101903y

De La Pierre, M., Carteret, C., Maschio, L., André, E., Orlando, R., & Dovesi, R. (2014). The Raman spectrum of CaCO 3 polymorphs calcite and aragonite: A combined experimental and computational study. The Journal of Chemical Physics, 140(16), 164509. https://doi.org/10.1063/1.4871900

De Leuw, S., Rubin, A. E., & Wasson, J. T. (2010). Carbonates in CM chondrites: Complex formational histories and comparison to carbonates in CI chondrites. Meteoritics & Planetary Science, 45(4), 513–530. https://doi.org/10.1111/j.1945-5100.2010.01037.x

DellaGiustina, D. N., Burke, K. N., Walsh, K. J., Smith, P. H., Golish, D. R., Bierhaus, E. B., Ballouz, R.-L., Becker, T. L., Campins, H., Tatsumi, E., Yumoto, K., Sugita, S., Deshapriya, J. D. P., Cloutis, E. A., Clark, B. E., Hendrix, A. R., Sen, A., Al Asad, M. M., Daly, M. G., … Lauretta, D. S. (2020). Variations in color and reflectance on the surface of asteroid (101955) Bennu. Science, 370(6517), eabc3660. https://doi.org/10.1126/science.abc3660

Della Porta, G., Hoppert, M., Hallmann, C., Schneider, D., & Reitner, J. (2022). The influence of microbial mats on travertine precipitation in active hydrothermal systems (Central Italy). The Depositional Record, 8(1), 165–209. https://doi.org/10.1002/dep2.147

Dupraz, C., Reid, R. P., Braissant, O., Decho, A. W., Norman, R. S., & Visscher, P. T. (2009). Processes of carbonate precipitation in modern microbial mats. Earth-Science Reviews, 96(3), 141–162. https://doi.org/10.1016/j.earscirev.2008.10.005

Edwards, H. G. M., Villar, S. E. J., Jehlicka, J., & Munshi, T. (2005). FT-Raman spectroscopic study of calcium-rich and magnesium-rich carbonate minerals. Spectrochimica Acta. Part A, Molecular and Biomolecular Spectroscopy, 61(10), 2273–2280. https://doi.org/10.1016/j.saa.2005.02.026

Ehlmann, B. L., Mustard, J. F., Murchie, S. L., Poulet, F., Bishop, J. L., Brown, A. J., Calvin, W. M., Clark, R. N., Marais, D. J. D., Milliken, R. E., Roach, L. H., Roush, T. L., Swayze, G. A., & Wray, J. J. (2008). Orbital identification of carbonate-bearing rocks on Mars. Science, 322(5909), Article 5909. https://doi.org/10.1126/science.1164759

Ehlmann, B. L., Mustard, J. F., Swayze, G. A., Clark, R. N., Bishop, J. L., Poulet, F., Des Marais, D. J., Roach, L. H., Milliken, R. E., Wray, J. J., Barnouin-Jha, O., & Murchie, S. L. (2009). Identification of hydrated silicate minerals on Mars using MRO-CRISM: Geologic context near Nili Fossae and implications for aqueous alteration. Journal of Geophysical Research: Planets, 114(E2). https://doi.org/10.1029/2009JE003339

Ehlmann, B. L., Mustard, J. F., & Murchie, S. L. (2010). Geologic setting of serpentine deposits on Mars. Geophysical Research Letters, 37(6). https://doi.org/10.1029/2010GL042596

Emerson, J. B., Thomas, B. C., Alvarez, W., & Banfield, J. F. (2016). Metagenomic analysis of a high carbon dioxide subsurface microbial community populated by chemolithoautotrophs and bacteria and archaea from candidate phyla. Environmental Microbiology, 18(6), 1686–1703. https://doi.org/10.1111/1462-2920.12817

Faatz, M., Gröhn, F., & Wegner, G. (2004). Amorphous calcium carbonate: Synthesis and potential intermediate in biomineralization. Advanced Materials, 16(12), 996–1000. https://doi.org/10.1002/adma.200306565

Farley, K. A., Williford, K. H., Stack, K. M., Bhartia, R., Chen, A., de la Torre, M., Hand, K., Goreva, Y., Herd, C. D. K., Hueso, R., Liu, Y., Maki, J. N., Martinez, G., Moeller, R. C., Nelessen, A., Newman, C. E., Nunes, D., Ponce, A., Spanovich, N., … Wiens, R. C. (2020). Mars 2020 mission overview. Space Science Reviews, 216(8), 142. https://doi.org/10.1007/s11214-020-00762-y

Faust, G.T. (1950) Thermal analysis studies on carbonates, I-aragonite and calcite. The American Mineralogist, 35, 207-224.

Ferrone, S. M., Clark, B. E., Kaplan, H. H., Rizos, J.-L., Zou, X.-D., Li, J.-Y., Barucci, M. A., Simon, A. A., Reuter, D., Hasselmann, P. H., Deshapriya, J. D. P., Poggiali, G., Brucato, J. R., Cambioni, S., Cloutis, E., Hamilton, V. E., & Lauretta, D. S. (2021). Visible–near-infrared observations of organics and carbonates on (101955) Bennu: Classification method and search for surface context. Icarus, 368, 114579. https://doi.org/10.1016/j.icarus.2021.114579

Finch, A., & Allison, N. (2007). Coordination of Sr and Mg in calcite and aragonite. Mineralogical Magazine - MINER MAG, 71, 539–552. https://doi.org/10.1180/minmag.2007.071.5.539

Folk, R. (1994). Interaction between bacteria, nannobacteria, and mineral precipitation in hot springs of central Italy. Géographie Physique et Quaternaire, 48(3), 233–246. https://doi.org/10.7202/033005ar

Ford, D. C. (2006). Aragonite cave deposits. In Encyclopedia of caves (pp. 27-33). Academic Press. https://doi.org/10.1016/B0-12-369396-9/00013-1

Fouchet, T., Reess, J.-M., Montmessin, F., Hassen-Khodja, R., Nguyen-Tuong, N., Humeau, O., Jacquinod, S., Lapauw, L., Parisot, J., Bonafous, M., Bernardi, P., Chapron, F., Jeanneau, A., Collin, C., Zeganadin, D., Nibert, P., Abbaki, S., Montaron, C., Blanchard, C., … Wiens, R. C. (2021). The SuperCam infrared spectrometer for the perseverance rover of the Mars2020 mission. Icarus, 114773. https://doi.org/10.1016/j.icarus.2021.114773

Gaffey, S. J. (1985). Reflectance spectroscopy in the visible and near-infrared (0.35 2.55 μm): Applications in carbonate petrology. Geology, 13, 270. https://doi.org/10.1130/0091-7613(1985)13<270:RSITVA>2.0.CO;2

Gaffey, S. J. (1987). Spectral reflectance of carbonate minerals in the visible and near infrared (0.35–2.55 um): Anhydrous carbonate minerals. Journal of Geophysical Research: Solid Earth, 92(B2), 1429–1440. https://doi.org/10.1029/JB092iB02p01429

Giralt, S., Julià, R., & Klerkx, J. (2001). Microbial biscuits of vaterite in lake Issyk-Kul (Republic of Kyrgyzstan). Journal of Sedimentary Research, 71(3), 430–435. https://doi.org/10.1306/2DC40951-0E47-11D7-8643000102C1865D

Glein, C. R., Baross, J. A., & Waite, J. H. (2015). The pH of Enceladus' ocean. Geochimica et Cosmochimica Acta, 162, 202–219. https://doi.org/10.1016/j.gca.2015.04.017

Glein, C. R., & Waite, J. H. (2020). The carbonate geochemistry of Enceladus' ocean. Geophysical Research Letters, 47(3). https://doi.org/10.1029/2019GL085885

Gibson, E. K., McKay, D. S., Thomas-Keprta, K. L., Wentworth, S. J., Westall, F., Steele, A., Romanek, C. S., Bell, M. S., & Toporski, J. (2001). Life on Mars: Evaluation of the evidence within Martian meteorites ALH84001, Nakhla, and Shergotty. Precambrian Research, 106(1), 15–34. https://doi.org/10.1016/S0301-9268(00)00122-4

Golden, D. C., Ming, D. W., Schwandt, C. S., Lauer, H. V., Jr., Socki, R. A., Morris, R. V., Lofgren, G. E., & McKay, G. A. (2001). A simple inorganic process for formation of

carbonates, magnetite, and sulfides in Martian meteorite ALH84001. American Mineralogist, 86(3), 370–375. https://doi.org/10.2138/am-2001-2-321

Goudge, T. A., Mustard, J. F., Head, J. W., Fassett, C. I., & Wiseman, S. M. (2015). Assessing the mineralogy of the watershed and fan deposits of the Jezero crater paleolake system, Mars. Journal of Geophysical Research: Planets, 120(4), 775–808. https://doi.org/10.1002/2014JE004782

Goudge, T. A., Milliken, R. E., Head, J. W., Mustard, J. F., & Fassett, C. I. (2017). Sedimentological evidence for a deltaic origin of the western fan deposit in Jezero crater, Mars and implications for future exploration. Earth and Planetary Science Letters, 458, 357–365. https://doi.org/10.1016/j.epsl.2016.10.056

Gouveia, F. J., Johnson, M. R., Leif, R. N., & Friedmann, S. J. (2005). Aerometric measurement and modeling of the mass of CO_2 emissions from Crystal Geyser, Utah (UCRL-TR-211870). Lawrence Livermore National Lab., Livermore, CA (US). https://doi.org/10.2172/15016180

Gouveia, F., & Friedmann, S. (2006). Timing and prediction of CO_2 eruptions from Crystal Geyser, UT (UCRL-TR-221731, 897988; p. UCRL-TR-221731, 897988). https://doi.org/10.2172/897988

Govindaraju, K. (1994). 1994 compilation of working values and sample description for 383 geostandards. Geostandards Newsletter, 18(S1), 1–158. https://doi.org/10.1046/j.1365-2494.1998.53202081.x-i1

Grotzinger, J. P., Crisp, J., Vasavada, A. R., Anderson, R. C., Baker, C. J., Barry, R., Blake, D. F., Conrad, P., Edgett, K. S., Ferdowski, B., Gellert, R., Gilbert, J. B., Golombek, M., Gómez-Elvira, J., Hassler, D. M., Jandura, L., Litvak, M., Mahaffy, P., Maki, J., … Wiens, R. C. (2012). Mars Science Laboratory mission and science investigation. Space Science Reviews, 170(1–4), 5–56. https://doi.org/10.1007/s11214-012-9892-2

Gruver, R. M. (1950). Differential thermal-analysis studies of ceramic materials: II, transition of aragonite to calcite. Journal of the American Ceramic Society, 33(5), 171–174. https://doi.org/10.1111/j.1151-2916.1950.tb12783.x

Halevy, I., Fischer, W. W., & Eiler, J. M. (2011). Carbonates in the Martian meteorite Allan Hills 84001 formed at 18 +/- 4 degrees C in a near-surface aqueous environment. Proceedings of the National Academy of Sciences of the United States of America, 108(41), 16895–16899. https://doi.org/10.1073/pnas.1109444108

Han, W. S., Watson, Z. T., Kampman, N., Grundl, T., Graham, J. P., & Keating, E. H. (2017). Periodic changes in effluent chemistry at cold-water geyser: Crystal geyser in Utah. Journal of Hydrology, 550, 54–64. https://doi.org/10.1016/j.jhydrol.2017.04.030

Hansen, C. J., Shemansky, D. E., Esposito, L. W., Stewart, A. I. F., Lewis, B. R., Colwell, J. E., Hendrix, A. R., West, R. A., Waite Jr., J. H., Teolis, B., & Magee, B. A. (2011). The composition and structure of the Enceladus plume. Geophysical Research Letters, 38(11). https://doi.org/10.1029/2011GL047415

Hays, L. E., Graham, H. V., Des Marais, D. J., Hausrath, E. M., Horgan, B., McCollom, T. M., Parenteau, M. N., Potter-McIntyre, S. L., Williams, A. J., & Lynch, K. L. (2017). Biosignature preservation and detection in Mars analog environments. Astrobiology, 17(4), 363–400. https://doi.org/10.1089/ast.2016.1627

Heath, J.E. (2004) *Hydrogeochemical characterization of leaking carbon dioxide-charged fault zones in east-central Utah* [Graduate Thesis, Utah State College].

Hendrix, A. R., Hurford, T. A., Barge, L. M., Bland, M. T., Bowman, J. S., Brinckerhoff, W., Buratti, B. J., Cable, M. L., Castillo-Rogez, J., Collins, G. C., Diniega, S., German, C. R., Hayes, A. G., Hoehler, T., Hosseini, S., Howett, C. J. A., McEwen, A. S., Neish, C. D.,

Neveu, M., … Vance, S. D. (2019). The NASA roadmap to ocean worlds. Astrobiology, 19(1), 1–27. https://doi.org/10.1089/ast.2018.1955

Hicks, L. J., Bridges, J. C., & Gurman, S. J. (2014). Ferric saponite and serpentine in the nakhlite martian meteorites. Geochimica et Cosmochimica Acta, 136, 194–210. https://doi.org/10.1016/j.gca.2014.04.010

Hill, C., & Forti, P. (1997). Cave minerals of the world. National Speleological Society Inc., Huntsville, Alabama.

Hoehler, T. M., & Westall, F. (2010). Mars Exploration Program Analysis Group goal one: determine if life ever arose on mars. Astrobiology, 10(9), 859–867. https://doi.org/10.1089/ast.2010.0527

Holland, H. D., Kirsipu, T. V., Huebner, J. S., & Oxburgh, U. M. (1964). On some aspects of the chemical evolution of cave waters. The Journal of Geology, 72(1), 36–67. https://doi.org/10.1086/626964

Horgan, B. H. N., Anderson, R. B., Dromart, G., Amador, E. S., & Rice, M. S. (2020). The mineral diversity of Jezero crater: Evidence for possible lacustrine carbonates on Mars. Icarus, 339, 113526. https://doi.org/10.1016/j.icarus.2019.113526

Horton, T., Atkinson, L., & Oze, C. (2012). Hydrothermal carbonate geochemistry of the Ngatamariki Subsurface Reservoir New Zealand. PROCEEDINGS, 37th Workshop on Geothermal Reservoir Engineering, Stanford University.

Jones, B. (2017). Review of calcium carbonate polymorph precipitation in spring systems. Sedimentary Geology, 353, 64–75. https://doi.org/10.1016/j.sedgeo.2017.03.006

Jones, B., & Renaut, R. W. (2010). Calcareous spring deposits in continental settings. In A. M. Alonso-Zarza & L. H. Tanner (Eds.), Developments in Sedimentology (Vol. 61, pp. 177–224). Elsevier. https://doi.org/10.1016/S0070-4571(09)06104-4

Josset, J.-L., Westall, F., Hofmann, B. A., Spray, J., Cockell, C., Kempe, S., Griffiths, A. D., De Sanctis, M. C., Colangeli, L., Koschny, D., Föllmi, K., Verrecchia, E., Diamond, L., Josset, M., Javaux, E. J., Esposito, F., Gunn, M., Souchon-Leitner, A. L., Bontognali, T. R. R., … Vago, J. L. (2017). The close-up imager onboard the ESA ExoMars Rover: Objectives, description, operations, and science validation activities. Astrobiology, 17(6–7), 595–611. https://doi.org/10.1089/ast.2016.1546

Kaplan, H. H., Lauretta, D. S., Simon, A. A., Hamilton, V. E., DellaGiustina, D. N., Golish, D. R., Reuter, D. C., Bennett, C. A., Burke, K. N., Campins, H., Connolly, H. C., Dworkin, J. P., Emery, J. P., Glavin, D. P., Glotch, T. D., Hanna, R., Ishimaru, K., Jawin, E. R., McCoy, T. J., … Enos, H. L. (2020). Bright carbonate veins on asteroid (101955) Bennu: Implications for aqueous alteration history. Science, 370(6517), eabc3557. https://doi.org/10.1126/science.abc3557

Khan, I., Rafiq, M., Zada, S., Jamil, S. U. U., & Hasan, F. (2021). Calcium carbonate precipitation by rock dwelling bacteria in Murree Hills, Lower Himalaya Range Pakistan. Geomicrobiology Journal, 38(3), 231–236. https://doi.org/10.1080/01490451.2020.1836085

Kivelson, M. G., Khurana, K. K., Russell, C. T., Volwerk, M., Walker, R. J., & Zimmer, C. (2000). Galileo magnetometer measurements: A stronger case for a subsurface ocean at Europa. Science, 289(5483), 1340–1343. https://doi.org/10.1126/science.289.5483.1340

Knuth, J. M., & Potter-McIntyre, S. L. (2021). Stable isotope fractionation in a cold spring system, Utah, USA: Insights for Sample Selection on Mars. Astrobiology, 21(2), 235–245. https://doi.org/10.1089/ast.2019.2028

Lea, D.W. (2003) Elemental and isotopic proxies of marine temperatures. Pp. 365390 in: The Oceans and Marine Geochemistry (H. Elderfield, editor). Treatise on Geochemistry, 6, Elsevier-Pergamon, Oxford, UK.

Lee, M. R., Lindgren, P., & Sofe, M. R. (2014). Aragonite, breunnerite, calcite and dolomite in the CM carbonaceous chondrites: High fidelity recorders of progressive parent body aqueous alteration. Geochimica et Cosmochimica Acta, 144, 126–156. https://doi.org/10.1016/j.gca.2014.08.019

Lippmann, F. (1973). Crystal chemistry of sedimentary carbonate minerals. In F. Lippmann (Ed.), Sedimentary Carbonate Minerals (pp. 5–96). Springer. https://doi.org/10.1007/978-3-642-65474-9_2

Loizeau, D., Pilorget, C., Riu, L., Brunetto, R., Bibring, J.-P., Nakato, A., Aléon-Toppani, A., Hatakeda, K., Yogata, K., Carter, J., Le Pivert-Jolivet, T., Yada, T., Okada, T., Usui, T., Langevin, Y., Lantz, C., Baklouti, D., Miyazaki, A., Nishimura, M., … Watanabe, S. (2023). Constraints on Solar System early evolution by MicrOmega analysis of Ryugu carbonates. Nature Astronomy, 1–7. https://doi.org/10.1038/s41550-022-01870-1

Lorenz, R. D. (2016). Europa ocean sampling by plume flythrough: Astrobiological expectations. Icarus, 267, 217–219. https://doi.org/10.1016/j.icarus.2015.12.018

Loste, E., Wilson, R. M., Seshadri, R., & Meldrum, F. C. (2003). The role of magnesium in stabilising amorphous calcium carbonate and controlling calcite morphologies. Journal of Crystal Growth, 254(1), 206–218. https://doi.org/10.1016/S0022-0248(03)01153-9

Lowenstam, H. A., & Weiner, S. (1983). Mineralization by organisms and the evolution of biomineralization. In Biomineralization and biological metal accumulation (pp. 191-203). Springer, Dordrecht. https://doi.org/10.1007/978-94-009-7944-4_17

Malesani, P., & Vannucci, S. (1975). Precipitazione di calcite o di aragonite dalle acque termominerali in relazione alla genesi e all'evoluzione dei travertini. Atti Della Accademia Nazionale Dei Lincei. Classe Di Scienze Fisiche, Matematiche e Naturali. Rendiconti, 59, 761–776.

Mandon, L., Quantin-Nataf, C., Royer, C., Beck, P., Fouchet, T., Johnson, J., Dehouck, E., Mouélic, S., Poulet, F., Montmessin, F., Pilorget, C., Gasnault, O., Forni, O., Mayhew, L., Beyssac, O., Bertrand, T., Clave, E., Pinet, P., Brown, A., & Wiens, R. (2023). Reflectance of Jezero crater floor: 2. Mineralogical interpretation. The Journal of Geophysical Research Planets. https://doi.org/10.1029/2022JE007450

Martinez Fadrique, F., Sánchez-Beato Fernández, R., Barrera, M., Franceschetti, P., & Joudrier, L. (2018). ExoMars 2020: Rover Operations Control System Design as part of the Rover Operations Control Center (ROCC). In 2018 SpaceOps Conference. American Institute of Aeronautics and Astronautics. https://doi.org/10.2514/6.2018-2405

Matsumoto, M., Fukunaga, T., & Onoe, K. (2010). Polymorph control of calcium carbonate by reactive crystallization using microbubble technique. Chemical Engineering Research and Design, 88(12), 1624–1630. https://doi.org/10.1016/j.cherd.2010.02.007

Maurice, S., Wiens, R. C., Bernardi, P., Caïs, P., Robinson, S., Nelson, T., Gasnault, O., Reess, J.-M., Deleuze, M., Rull, F., Manrique, J.-A., Abbaki, S., Anderson, R. B., André, Y., Angel, S. M., Arana, G., Battault, T., Beck, P., Benzerara, K., … Wong, K. W. (2021). The SuperCam instrument suite on the Mars 2020 Rover: Science Objectives and Mast-Unit Description. Space Science Reviews, 217(3), 47. https://doi.org/10.1007/s11214-021-00807-w

McCauley, J. W., & Roy, R. (1974). Controlled nucleation and crystal growth of various CaC03 phases by the silica gel technique. American Mineralogist, 59(9–10), 947–963.

McLennan, S. M., Sephton, M., Allen, C., Allwood, A., Barbieri, R., Beaty, D., Boston, P., Carr, M., Grady, M., Grant, J., Heber, V., Herd, C., Hofmann, B., King, P., Mangold, N., Ori, G.-G., Rossi, A. P., Raulin, F., Ruff, S., & Wilson (2012). Planning for Mars Returned Sample Science: Final report of the MSR End-to-End International Science Analysis Group (E2E-iSAG). Astrobiology, 12, 175–230. https://doi.org/10.1089/ast.2011.0805

McTigue, J. W., & Wenk, H-R. (1985). Microstructures and orientation relationships in the dry-state aragonite–calcite and calcite–lime phase transformations. American Mineralogist, 70(11–12), 1253–1261.

Meenakshi, V. R., Blackwelder, P. L., & Watabe, N. (1974). Studies on the formation of calcified egg-capsules of ampullarid snails. Calcified Tissue Research, 16(1), 283–291. https://doi.org/10.1007/BF02008236

Mertzman, S. (2000). K-Ar results from the southern Oregon-northern California Cascade Range. Oregon Geol., 62, 99–122.

Morris, R. V., Ruff, S. W., Gellert, R., Ming, D. W., Arvidson, R. E., Clark, B. C., Golden, D. C., Siebach, K., Klingelhöfer, G., Schröder, C., Fleischer, I., Yen, A. S., & Squyres, S. W. (2010). Identification of carbonate-rich outcrops on Mars by the Spirit Rover. Science, 329(5990), 421–424. https://doi.org/10.1126/science.1189667

Murray, J. W. (1954). The deposition of calcite and aragonite in Caves. The Journal of Geology, 62(5), 481–492. https://doi.org/10.1086/626192

Nakamura, T., Matsumoto, M., Amano, K., Enokido, Y., Zolensky, M. E., Mikouchi, T., Genda, H., Tanaka, S., Zolotov, M. Y., Kurosawa, K., Wakita, S., Hyodo, R., Nagano, H., Nakashima, D., Takahashi, Y., Fujioka, Y., Kikuiri, M., Kagawa, E., Matsuoka, M., … Tsuda, Y. (2022). Formation and evolution of carbonaceous asteroid Ryugu: Direct evidence from returned samples. Science, 379(6634), eabn8671. https://doi.org/10.1126/science.abn8671

Nakato, A., Yada, T., Nishimura, M., Yogata, K., Miyazaki, A., Nagashima, K., Hatakeda, K., Kumagai, K., Hitomi, Y., Soejima, H., Bibring, J.-P., Pilorget, C., Hamm, V., Brunetto, R., Riu, L., Lourit, L., Loizeau, D., Le Pivert-Jolivet, T., Lequertier, G., … Tsuda, Y. (2023). Variations of the surface characteristics of Ryugu returned samples. Earth, Planets and Space, 75(1), 45. https://doi.org/10.1186/s40623-022-01754-8

Neveu, M., Anbar, A. D., Davila, A. F., Glavin, D. P., MacKenzie, S. M., Phillips-Lander, C. M., Sherwood, B., Takano, Y., Williams, P., & Yano, H. (2020). Returning samples from Enceladus for life detection. Frontiers in Astronomy and Space Sciences, 7. https://doi.org/10.3389/fspas.2020.00026

Niles, P. B., Catling, D. C., Berger, G., Chassefière, E., Ehlmann, B. L., Michalski, J. R., Morris, R., Ruff, S. W., & Sutter, B. (2013). Geochemistry of carbonates on Mars: Implications for climate history and nature of aqueous environments. Space Science Reviews, 174(1), 301–328. https://doi.org/10.1007/s11214-012-9940-y

Ogino, T., Suzuki, T., & Sawada, K. (1987). The formation and transformation mechanism of calcium carbonate in water. Geochimica Et Cosmochimica Acta, 51(10), 2757–2767. https://doi.org/10.1016/0016-7037(87)90155-4

Okumura, T., Takashima, C., Shiraishi, F., Akmaluddin, & Kano, A. (2012). Textural transition in an aragonite travertine formed under various flow conditions at Pancuran Pitu, Central Java, Indonesia. Sedimentary Geology, 265–266, 195–209. https://doi.org/10.1016/j.sedgeo.2012.04.010

Oliveira, A. M., Farina, M., Ludka, I. P., & Kachar, B. (1996). Vaterite, calcite, and aragonite in the otoliths of three species of piranha. Naturwissenschaften, 83(3), 133–135. https://doi.org/10.1007/BF01142180

Orlando, T. M., McCord, T. B., & Grieves, G. A. (2005). The chemical nature of Europa surface material and the relation to a subsurface ocean. Icarus, 177(2), 528–533. https://doi.org/10.1016/j.icarus.2005.05.009

Palchik, N. A., & Moroz, T. N. (2005). Polymorph modifications of calcium carbonate in gallstones. Journal of Crystal Growth, 283(3), 450–456. https://doi.org/10.1016/j.jcrysgro.2005.05.035

Palomba, E., Zinzi, A., Cloutis, E. A., D'Amore, M., Grassi, D., & Maturilli, A. (2009). Evidence for Mg-rich carbonates on Mars from a 3.9μm absorption feature. Icarus, 203(1), 58–65. https://doi.org/10.1016/j.icarus.2009.04.013

Palomba, E., Longobardo, A., De Sanctis, M. C., Stein, N. T., Ehlmann, B., Galiano, A., Raponi, A., Ciarniello, M., Ammannito, E., Cloutis, E., Carrozzo, F. G., Capria, M. T., Stephan, K., Zambon, F., Tosi, F., Raymond, C. A., & Russell, C. T. (2019). Compositional differences among Bright Spots on the Ceres surface. Icarus, 320, 202–212. https://doi.org/10.1016/j.icarus.2017.09.020

Parker, J. E., Thompson, S. P., Lennie, A. R., Potter, J., & Tang, C. C. (2010). A study of the aragonite-calcite transformation using Raman spectroscopy, synchrotron powder diffraction and scanning electron microscopy. CrystEngComm, 12(5), 1590. https://doi.org/10.1039/b921487a

Pentecost, A. (2005). *Travertine*. Springer-Verlag Berlin Heidelberg.

Potter-McIntyre, S. (2019). Crystal Geyser: An unusual cold spring system, Grand County. Geosites, 1, 1–6. https://doi.org/10.31711/geosites.v1i1.63

Potter-McIntyre, S. L., Williams, J., Phillips-Lander, C., & O'Connell, L. (2017). Taphonomy of microbial biosignatures in spring deposits: A comparison of modern, quaternary, and Jurassic examples. Astrobiology, 17(3), 216–230. https://doi.org/10.1089/ast.2016.1495

Rao, M. S. (1973). Kinetics and mechanism of the transformation of vaterite to calcite. Bulletin of the Chemical Society of Japan, 46(5), 1414–1417. https://doi.org/10.1246/bcsj.46.1414

Raponi, A., De Sanctis, M. C., Carrozzo, F. G., Ciarniello, M., Castillo-Rogez, J. C., Ammannito, E., Frigeri, A., Longobardo, A., Palomba, E., Tosi, F., Zambon, F., Raymond, C. A., & Russell, C. T. (2019). Mineralogy of Occator crater on Ceres and insight into its evolution from the properties of carbonates, phyllosilicates, and chlorides. Icarus, 320, 83–96. https://doi.org/10.1016/j.icarus.2018.02.001

Reichen, L. E., 1916-, Fahey, J. J., & 1901-. (1962). Improved method for the determination of FeO in rocks and minerals including garnet. U.S. G.P.O. https://scholar.google.com/scholar_lookup?title=improved+method+for+the+determination+of+FeO+in+rocks+and+minerals+including+garnet&author=Reichen%2C+Laura+E.&publication_year=1962

Ren, F., Wan, X., Ma, Z., & Su, J. (2009). Study on microstructure and thermodynamics of nacre in mussel shell. Materials Chemistry and Physics, 114(1), 367–370. https://doi.org/10.1016/j.matchemphys.2008.09.036

Renaut, R. W., & Jones, B. (1997). Controls on aragonite and calcite precipitation in hot spring travertines at Chemurkeu, Lake Bogoria, Kenya. Canadian Journal of Earth Sciences, 34(6), Article 6. https://doi.org/10.1139/e17-066

Rice, M. S., Cloutis, E. A., Bell, J. F., Bish, D. L., Horgan, B. H., Mertzman, S. A., Craig, M. A., Renaut, R. W., Gautason, B., & Mountain, B. (2013). Reflectance spectra diversity of silica-rich materials: Sensitivity to environment and implications for detections on Mars. Icarus, 223(1), 499–533. https://doi.org/10.1016/j.icarus.2012.09.021

Simon, A. A., Kaplan, H. H., Hamilton, V. E., Lauretta, D. S., Campins, H., Emery, J. P., Barucci, M. A., DellaGiustina, D. N., Reuter, D. C., Sandford, S. A., Golish, D. R., Lim, L. F., Ryan,

A., Rozitis, B., & Bennett, C. A. (2020). Widespread carbon-bearing materials on near-Earth asteroid (101955) Bennu. Science, 370(6517), eabc3522. https://doi.org/10.1126/science.abc3522

Stalport, F., Coll, P., Szopa, C., Person, A., Navarro-González, R., Cabane, M., Ausset, P., & Vaulay, M. J. (2007). Search for past life on Mars: Physical and chemical characterization of minerals of biotic and abiotic origin: 2. Aragonite. Geophysical Research Letters, 34(24). https://doi.org/10.1029/2007GL031184

Santillan, E. F., Shanahan, T., Omelon, C., Major, J., & Bennett, P. (2015). Isolation and characterization of a CO_2-tolerant Lactobacillus strain from Crystal Geyser, Utah, U.S.A. Frontiers in Earth Science, 3, 41. https://doi.org/10.3389/feart.2015.00041

Scheinost, A. C., Chavernas, A., Barrón, V., & Torrent, J. (1998). Use and limitations of second-derivative diffuse reflectance spectroscopy in the visible to near-infrared range to identify and quantify Fe oxide minerals in soils. Clays and Clay Minerals, 46(5), 528–536. https://doi.org/10.1346/CCMN.1998.0460506

Schmidt, C., & Ziemann, M. (2000). In-situ Raman spectroscopy of quartz: A pressure sensor for hydrothermal diamond-anvil cell experiments at elevated temperatures. American Mineralogist, 85, 1725–1734. https://doi.org/10.2138/am-2000-11-1216

Shipton, Z. K., Evans, J. P., Kirchner, D., Kolesar, P. T., Williams, A. P., & Heath, J. (2004). Analysis of CO_2 leakage through "low-permeability" faults from natural reservoirs in the Colorado Plateau, southern Utah (S. J. Baines & R. H. Worden, Eds.; Vol. 233, pp. 43–58). Geological Society of London. https://eprints.gla.ac.uk/968/

Shipton, Z., Evans, J., Dockrill, B., Heath, J., Williams, A., Kirchner, D., & Kolesar, P. (2005). Natural leaking CO_2-charged systems as analogs for failed geologic storage reservoirs. In CCP Summary (Vol. 2, pp. 699–712). https://doi.org/10.1016/B978-008044570-0/50130-6

Siegel, F. R., & Reams, M. W. (1966). Temperature effect on precipitation of calcium carbonate from calcium bicarbonate solutions and its application to cavern environments. Sedimentology, 7(3), 241–248. https://doi.org/10.1111/j.1365-3091.1966.tb01597.x

Smith, D., Jenkin, G., Petterson, M., Naden, J., Fielder, S., Toba, T., & Chenery, S. (2011). Unusual mixed silica-carbonate deposits from magmatic-hydrothermal hot springs, Savo, Solomon Islands. Journal of the Geological Society, 168, 1297–1310. https://doi.org/10.1144/0016-76492011-003

Stack, K. M., Williams, N. R., Calef, F., Sun, V. Z., Williford, K. H., Farley, K. A., Eide, S., Flannery, D., Hughes, C., Jacob, S. R., Kah, L. C., Meyen, F., Molina, A., Nataf, C. Q., Rice, M., Russell, P., Scheller, E., Seeger, C. H., Abbey, W. J., … Aileen Yingst, R. (2020). Photogeologic map of the Perseverance Rover field site in Jezero crater constructed by the Mars 2020 science team. Space Science Reviews, 216(8), 127. https://doi.org/10.1007/s11214-020-00739-x

Steele, A., Fries, M. D., Amundsen, H. E. F., Mysen, B. O., Fogel, M. L., Schweizer, M., & Boctor, N. Z. (2007). Comprehensive imaging and Raman spectroscopy of carbonate globules from Martian meteorite ALH 84001 and a terrestrial analogue from Svalbard. Meteoritics & Planetary Science, 42(9), 1549–1566. https://doi.org/10.1111/j.1945-5100.2007.tb00590.x

Tai, C. Y., & Chen, F.-B. (1998). Polymorphism of CaCO3, precipitated in a constant-composition environment. AIChE Journal, 44(8), 1790–1798. https://doi.org/10.1002/aic.690440810

Takashima, C., Okumura, T., Nishida, S., Shimamoto, T., Koike, H., & Kano, A. (2011). Microbial control on lamina formation in a travertine of Crystal Geyser, Utah. In J. Reitner, N.-V. Quéric, & G. Arp (Eds.), Advances in Stromatolite Geobiology (pp. 123–133). Springer. https://doi.org/10.1007/978-3-642-10415-2_7

Tarnas, J. D., Stack, K. M., Parente, M., Koeppel, A. H. D., Mustard, J. F., Moore, K. R., Horgan, B. H. N., Seelos, F. P., Cloutis, E. A., Kelemen, P. B., Flannery, D., Brown, A. J., Frizzell, K. R., & Pinet, P. (2021). Characteristics, origins, and biosignature preservation potential of carbonate-bearing rocks within and outside of Jezero crater. Journal of Geophysical Research: Planets. https://doi.org/10.1029/2021JE006898

Teolis, B. D., Wyrick, D. Y., Bouquet, A., Magee, B. A., & Waite, J. H. (2017). Plume and surface feature structure and compositional effects on Europa's global exosphere: Preliminary Europa mission predictions. Icarus, 284, 18–29. https://doi.org/10.1016/j.icarus.2016.10.027

Toffolo, M. B., Ricci, G., Caneve, L., & Kaplan-Ashiri, I. (2019). Luminescence reveals variations in local structural order of calcium carbonate polymorphs formed by different mechanisms. Scientific Reports, 9(1), 1–15. https://doi.org/10.1038/s41598-019-52587-7

Tomić, Z., Makreski, P., & Gajić, B. (2010). Identification and spectra–structure determination of soil minerals: Raman study supported by IR spectroscopy and X-ray powder diffraction. Journal of Raman Spectroscopy, 41(5), 582–586. https://doi.org/10.1002/jrs.2476

Vecht, A., & Ireland, T. G. (2000). The role of vaterite and aragonite in the formation of pseudo-biogenic carbonate structures: Implications for Martian exobiology. Geochimica et Cosmochimica Acta, 64(15), 2719–2725. https://doi.org/10.1016/S0016-7037(00)00381-1

Veneranda, M., Lopez-Reyes, G., Manrique-Martinez, J. A., Sanz-Arranz, A., Lalla, E., Konstantinidis, M., Moral, A., Medina, J., & Rull, F. (2020). ExoMars Raman Laser Spectrometer (RLS): Development of chemometric tools to classify ultramafic igneous rocks on Mars. Scientific Reports, 10(1), 16954. https://doi.org/10.1038/s41598-020-73846-y

Vorburger, A., & Wurz, P. (2021). Modeling of possible plume mechanisms on Europa. Journal of Geophysical Research: Space Physics, 126(9), e2021JA029690. https://doi.org/10.1029/2021JA029690

Wade, L., Allwood, A., Foote, M., Dawson, D., Liebe, C., Ek, E., Schein, M., Pootrakul, S., Hernandez, B., Sharrow, R. (2016). Overview of the Mars 2020 mission micro-XRF instrument PIXL. 251st American Chemical Society National Meeting & Exposition, March 13-17, 2016, San Diego, CA; http://www.acs.org/content/acs/en/meetings/spring-2016.html

Waite, J. H., Combi, M. R., Ip, W.-H., Cravens, T. E., McNutt, R. L., Kasprzak, W., Yelle, R., Luhmann, J., Niemann, H., Gell, D., Magee, B., Fletcher, G., Lunine, J., & Tseng, W.-L. (2006). Cassini ion and neutral mass spectrometer: Enceladus plume composition and structure. Science, 311(5766), 1419–1422. https://doi.org/10.1126/science.1121290

Waltham, T. (2001). Crystal Geyser – Utah's cold one. Geology Today, 17(1), 22–24. https://doi.org/10.1046/j.1365-2451.2001.0008a.x

Wiens, R. C., Maurice, S., Barraclough, B., Saccoccio, M., Barkley, W. C., Bell, J. F., Bender, S., Bernardin, J., Blaney, D., Blank, J., Bouyé, M., Bridges, N., Bultman, N., Caïs, P., Clanton, R. C., Clark, B., Clegg, S., Cousin, A., Cremers, D., … Wong-Swanson, B. (2012). The ChemCam instrument suite on the Mars Science Laboratory (MSL) Rover: Body unit and combined system tests. Space Science Reviews, 170(1), 167–227. https://doi.org/10.1007/s11214-012-9902-4

Wolfe, A. P., Vinebrooke, R. D., Michelutti, N., Rivard, B., & Das, B. (2006). Experimental calibration of lake-sediment spectral reflectance to chlorophyll a concentrations: Methodology and paleolimnological validation. Journal of Paleolimnology, 36(1), 91–100. https://doi.org/10.1007/s10933-006-0006-6

Xu, Y., & Sommerdijk, N. A. J. M. (2018). Aragonite formation in confinements: A step toward understanding polymorph control. Proceedings of the National Academy of Sciences, 115(34), 8469–8471. https://doi.org/10.1073/pnas.1811696115

Yokoyama, T., Nagashima, K., Nakai, I., Young, E. D., Abe, Y., Aléon, J., Alexander, C. M. O., Amari, S., Amelin, Y., Bajo, K., Bizzarro, M., Bouvier, A., Carlson, R. W., Chaussidon, M., Choi, B.-G., Dauphas, N., Davis, A. M., Di Rocco, T., Fujiya, W., … Yurimoto, H. (2022). Samples returned from the asteroid Ryugu are similar to Ivuna-type carbonaceous meteorites. Science, 379(6634), eabn7850. https://doi.org/10.1126/science.abn7850

Zastrow, A. M., & Glotch, T. D. (2021). Distinct carbonate lithologies in Jezero Crater, Mars. Geophysical Research Letters, 48(9), e2020GL092365. https://doi.org/10.1029/2020GL092365

Zentilli, M., Omelon, C. R., Hanley, J., & LeFort, D. (2019). Paleo-hydrothermal predecessor to perennial spring activity in thick permafrost in the Canadian high arctic, and its relation to deep salt structures: Expedition Fiord, Axel Heiberg Island, Nunavut. Geofluids, 2019, e9502904. https://doi.org/10.1155/2019/9502904

Zhang, J., Zhao, C., Zhou, A., Yang, C., Zhao, L., & Li, Z. (2019). Aragonite formation induced by open cultures of microbial consortia to heal cracks in concrete: Insights into healing mechanisms and crystal polymorphs. Construction and Building Materials, 224, 815–822. https://doi.org/10.1016/j.conbuildmat.2019.07.129

Zhang, Q., Zhang, F., Zhao, Y., Yu, X., & Zhang, X. (2020). Biomineralization and biogenic aragonite formation in mollusks: A review. Journal of Oceanology and Limnology, 38(2), 285-297. https://doi.org/10.1007/s00343-019-8323-9

Zolotov, M. Y. (2007). An oceanic composition on early and today's Enceladus. Geophysical Research Letters, 34(23). https://doi.org/10.1029/2007GL031234

Zolotov, M. Y., & Shock, E. L. (2004). A model for low-temperature biogeochemistry of sulfur, carbon, and iron on Europa. Journal of Geophysical Research: Planets, 109(E6). https://doi.org/10.1029/2003JE002194

11.0 Supplemental material

1. Raman spectra of each target (Excel)
2. Reflectance spectra of each target (Excel)

Appendix

Rock samples from Utah Crystal Geyser site were crushed and dry-sieved to grain size of <45 µm. Below is the X-ray diffraction spectra for each sample, UTE001 to UTE011.

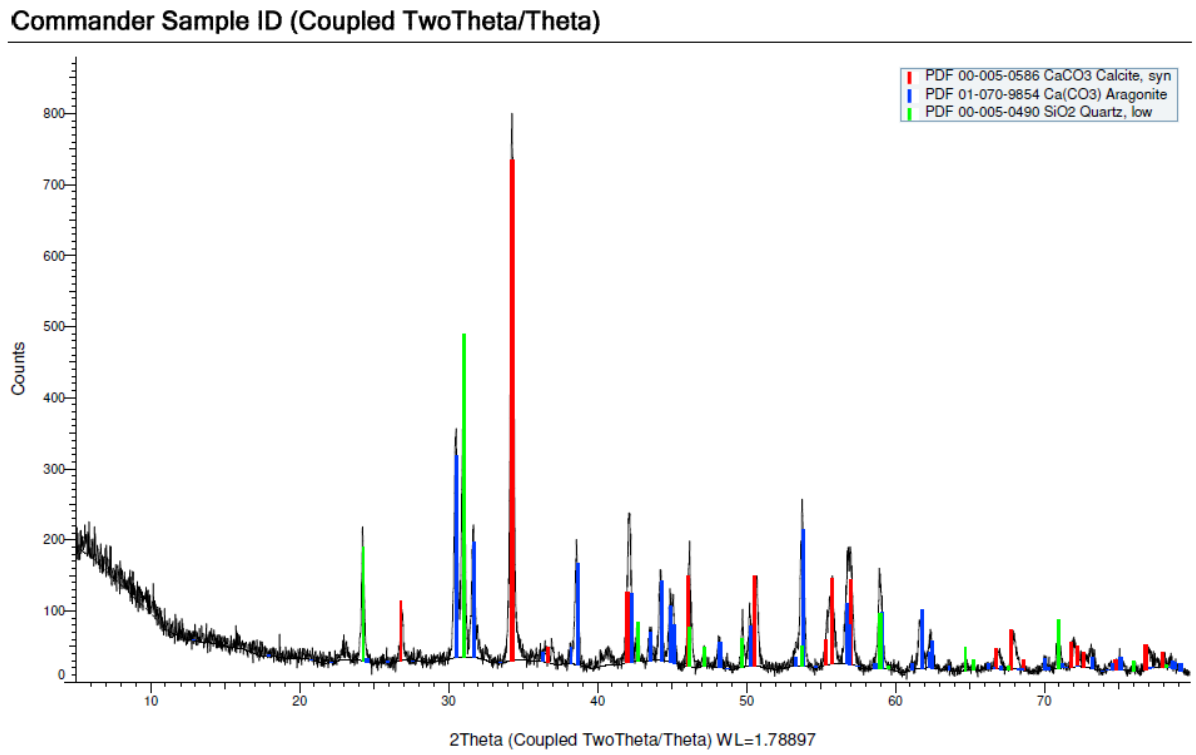

Figure A 1: XRD spectrum for sample number UTE001. Analysis was conducted on powder <45 µm.

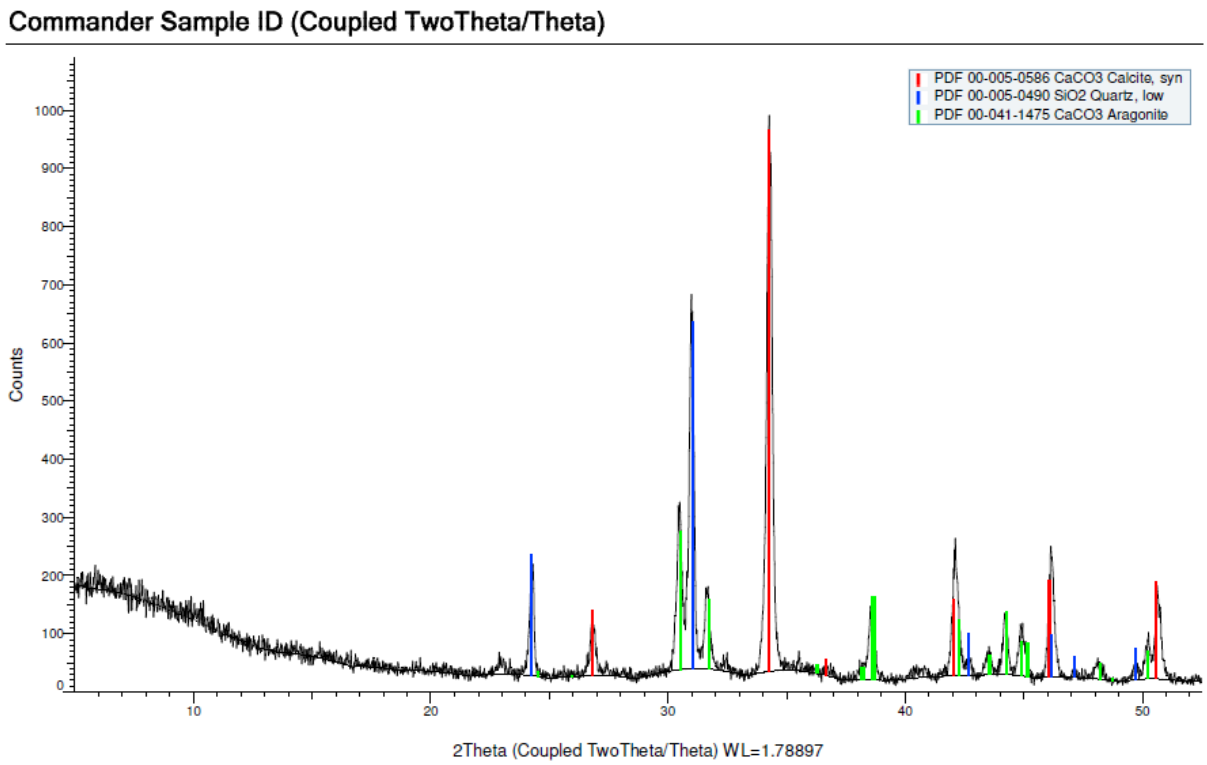

Figure A 2: XRD spectrum for sample number UTE002. Analysis was conducted on powder <45 µm.

.

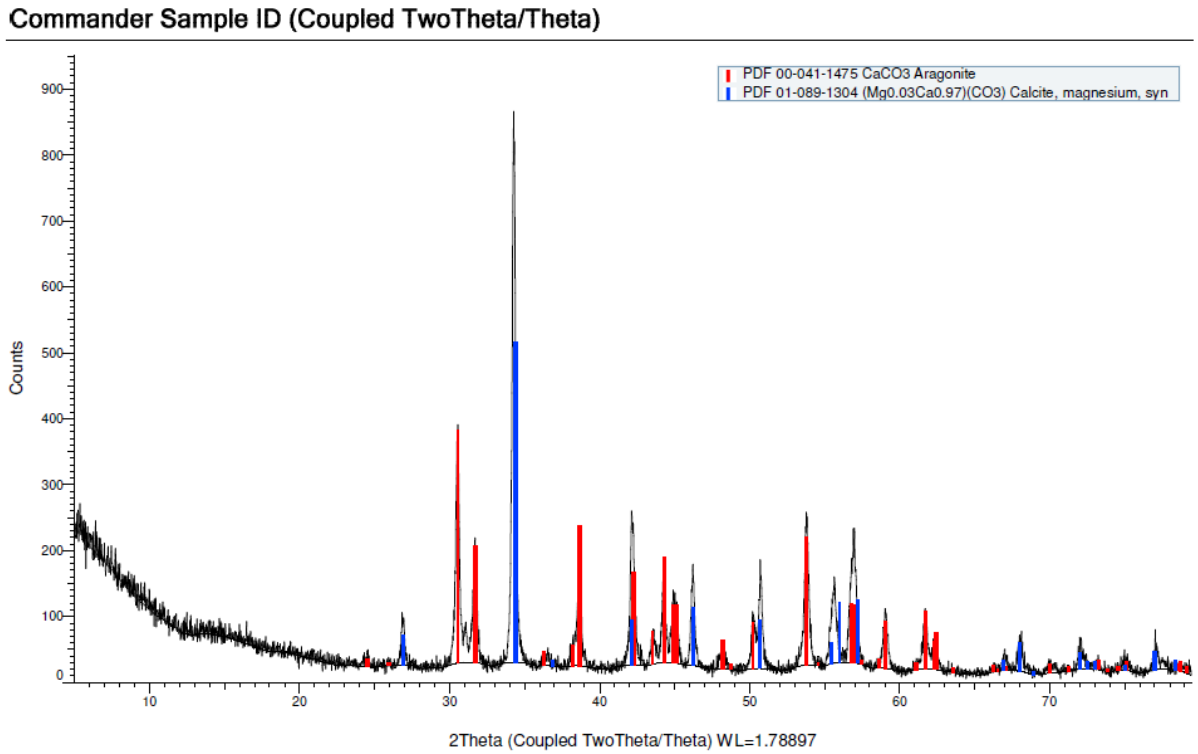

Figure A 3: XRD spectrum for sample number UTE003. Analysis was conducted on powder <45 µm.

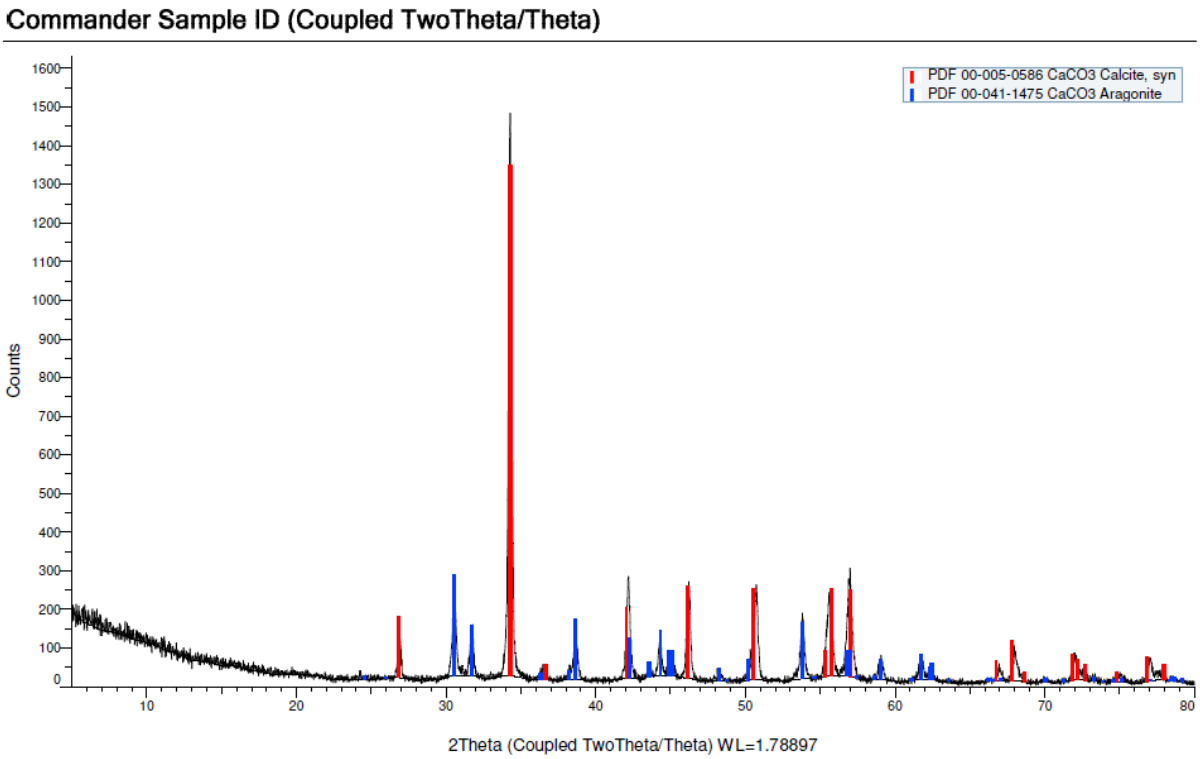

Figure A 4: XRD spectrum for sample number UTE004. Analysis was conducted on powder <45 µm.

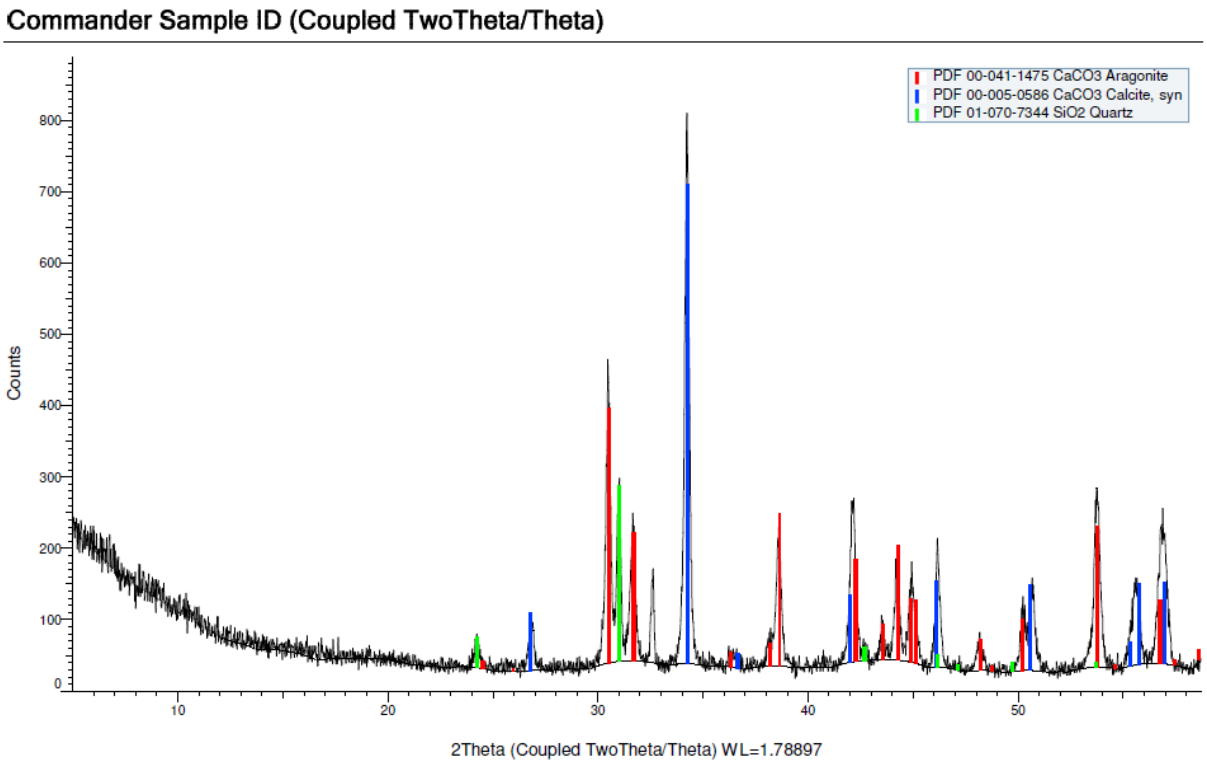

Figure A 5: XRD spectrum for sample number UTE005. Analysis was conducted on powder <45 µm.

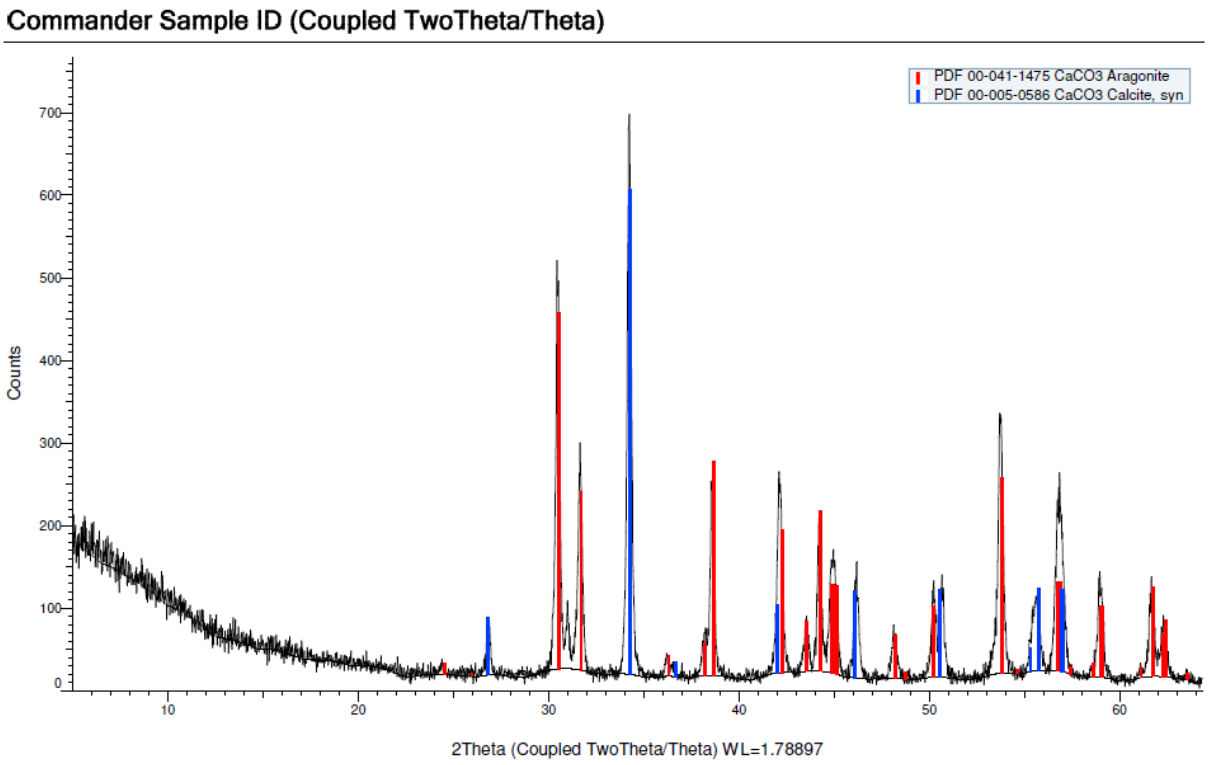

Figure A 6: XRD spectrum for sample number UTE006. Analysis was conducted on powder <45 µm.

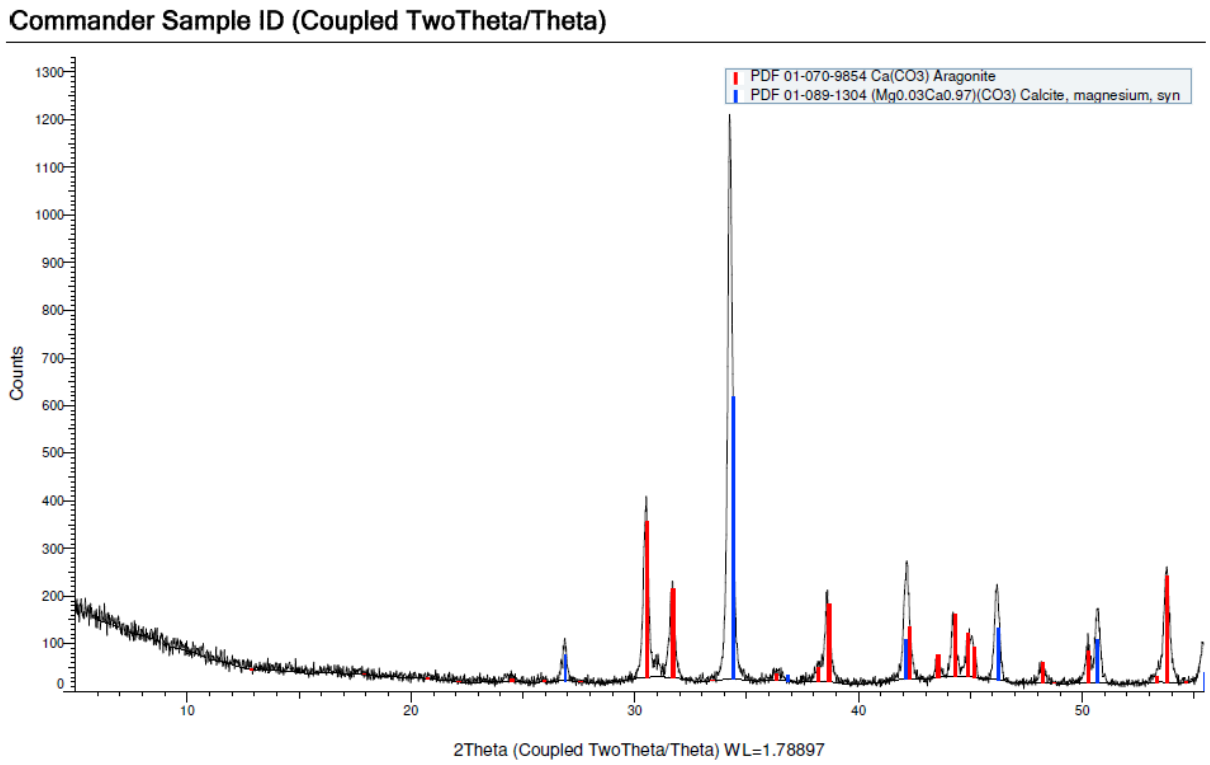

Figure A 7: XRD spectrum for sample number UTE007. Analysis was conducted on powder <45 μm.

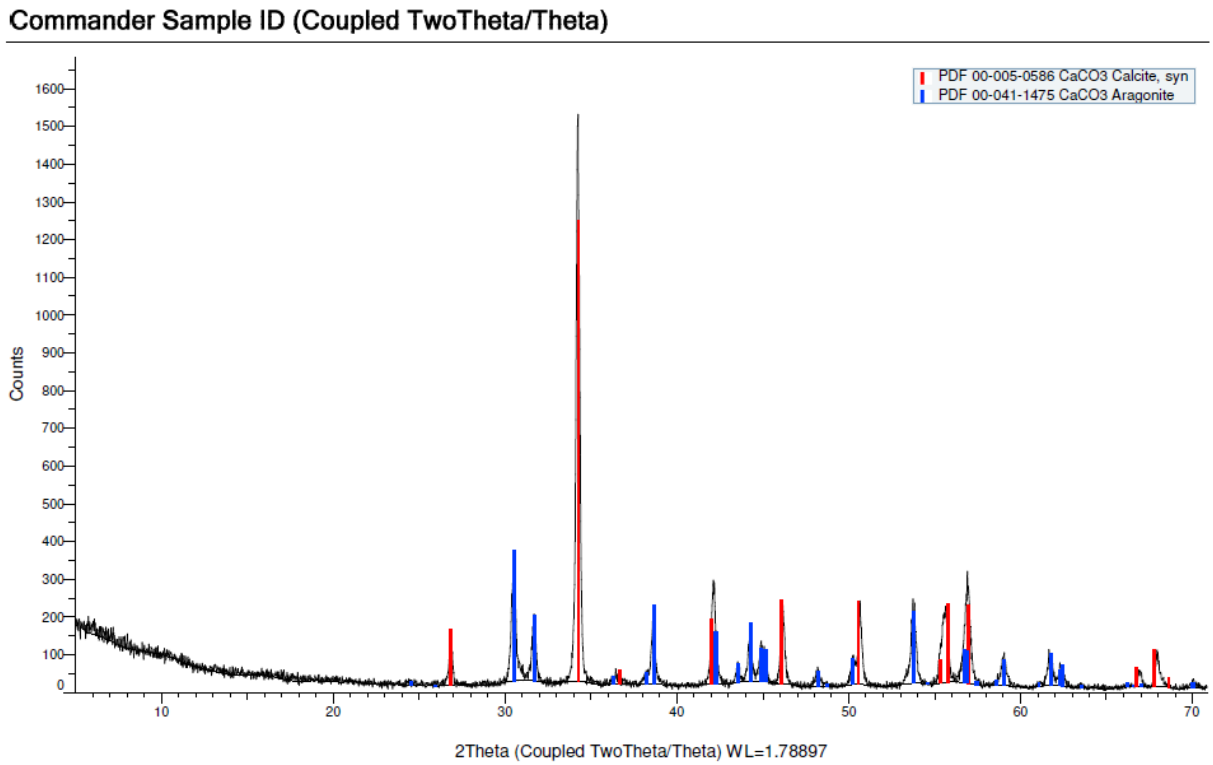

Figure A 8: XRD spectrum for sample number UTE008. Analysis was conducted on powder <45 µm.

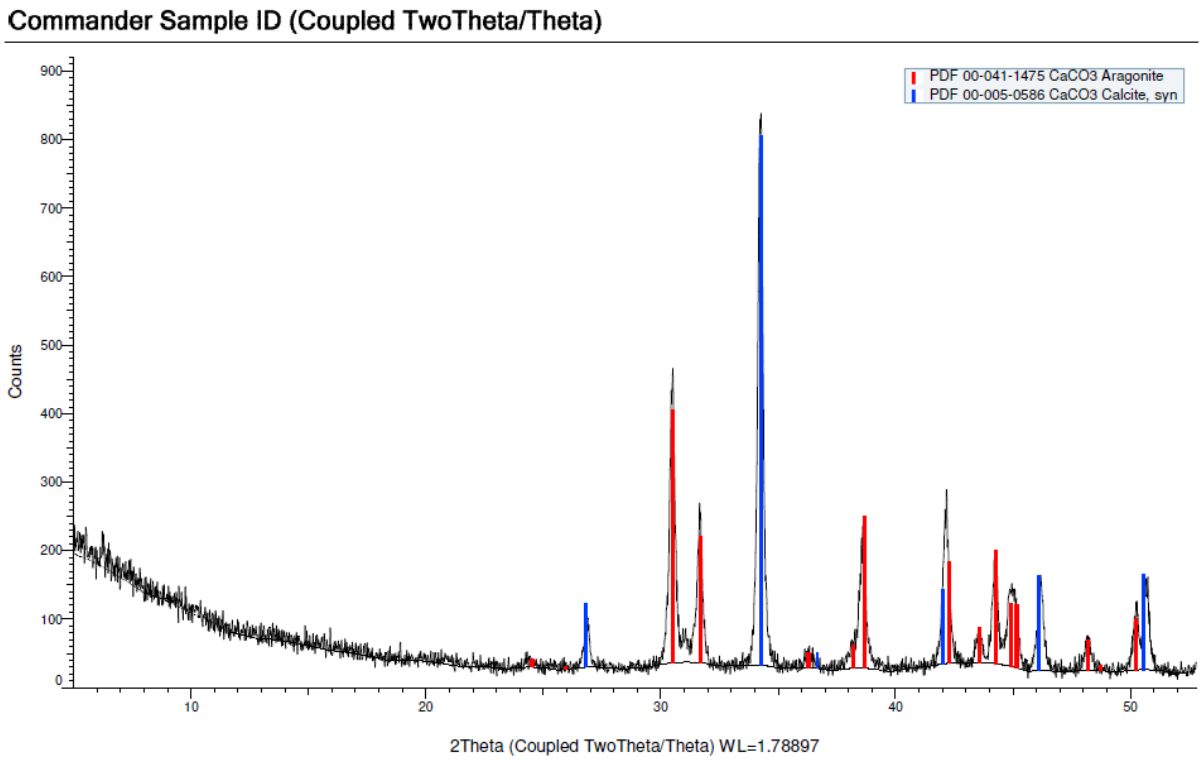

Figure A 9: XRD spectrum for sample number UTE009. Analysis was conducted on powder <45 µm.

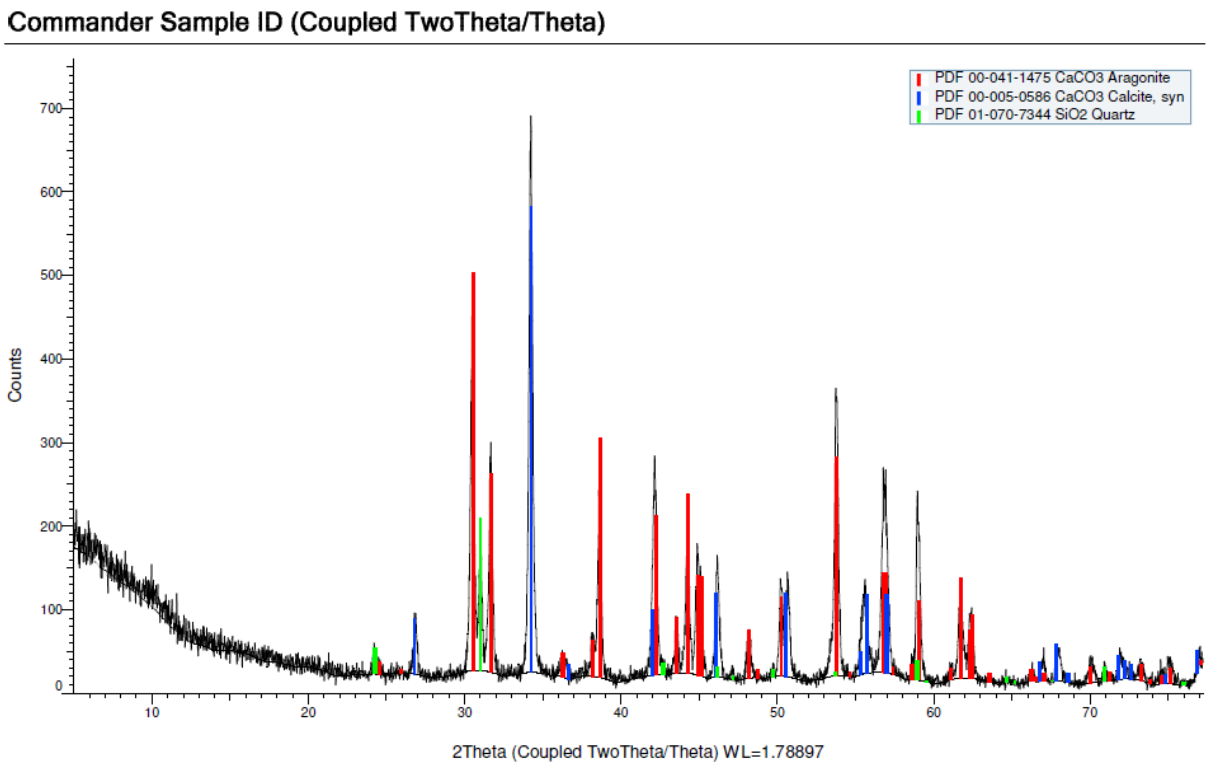

Figure A 10: XRD spectrum for sample number UTE010. Analysis was conducted on powder <45 µm.

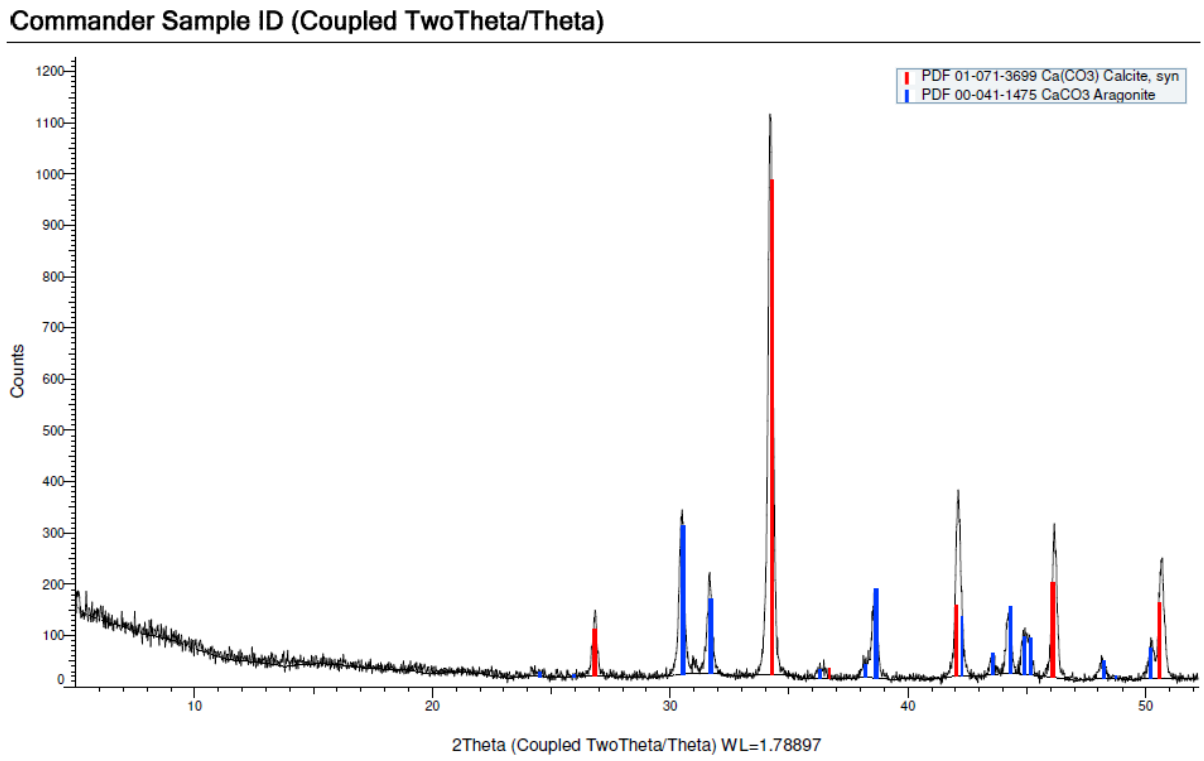

Figure A 11: XRD spectrum for sample number UTE011. Analysis was conducted on powder <45 µm.